

## Search for and analysis of eclipsing binaries in the LAMOST Medium-Resolution Survey field. I. RA: $23^h01^m51^s$ , Dec: $+34^\circ36'45''$

JING-YI WANG,<sup>1</sup> KAI LI,<sup>1</sup> XIANG GAO,<sup>1</sup> DI-FU GUO,<sup>1</sup> LI-HENG WANG,<sup>1</sup> DONG-YANG GAO,<sup>1</sup> LING-ZHI LI,<sup>1</sup> YA-NI GUO,<sup>1</sup> XING GAO,<sup>2</sup> AND GUO-YOU SUN<sup>3</sup>

<sup>1</sup>*Shandong Key Laboratory of Optical Astronomy and Solar-Terrestrial Environment, School of Space Science and Technology, Institute of Space Sciences, Shandong University, Weihai, Shandong, 264209, China*

<sup>2</sup>*Xinjiang Astronomical Observatory, 150 Science 1-Street, Urumqi 830011, China*

<sup>3</sup>*Xingming Observatory, Urumqi, Xinjiang, China*

Submitted to ApJ

### ABSTRACT

Eclipsing binaries (EBs) play an important astrophysical role in studying stellar properties and evolution. By analyzing photometric data in the LAMOST Medium-Resolution Survey field, RA:  $23^h01^m51.00^s$ , Dec:  $+34^\circ36'45''$ , 48 EBs are detected and 2 are newly discovered. This specific field has been observed 52 times by the LAMOST Medium-Resolution Survey DR 9, which facilitates a comprehensive analysis of the EBs. For EBs with LAMOST medium-resolution spectra, radial velocity curves were obtained, and their precise orbital parameters were determined by simultaneously analyzing photometric light curves and radial velocity curves. For the other EBs with only photometric light curves, we used the q-search or the temperature ratio method to determine their initial mass ratios and then determined the orbital parameters. It is found that 15 EBs belong to detached systems, 1 to semi-detached systems, and 32 to contact systems. Based on the O-C analysis for 26 EBs with sufficient eclipsing times, we found a long-term decrease in the orbital period of 11 EBs and a continuous increase of 5 EBs, which are due to the material transfer between the two components. The O-C curve of 1 EB shows a distinct periodic variation, which is caused by the light travel time effect, and the third body is likely to be a black hole. By applying the spectral subtraction method to 13 EBs with LAMOST medium-resolution spectra, 10 systems exhibit distinct H $\alpha$  emission lines, in which 1 system exhibits double-peaked lines near phases 0.25 and 0.75, implying strong chromospheric activity. In the mass-luminosities and mass-radius distributions, most of the more massive components are less evolved than the less massive ones.

*Keywords:* stars: binaries: close — stars: binaries: eclipsing — stars: fundamental parameters — stars: evolution — stars: chromospheric activity

### 1. INTRODUCTION

Variable stars are stars whose brightness varies over time, either due to intrinsic physical factors, such as pulsations and eruptions, or due to extrinsic factors, such as eclipses (Mattei & Saladyga 1999). Among variable stars, EBs play an important astrophysical role. The study of EBs is crucial for the precise determination of the fundamental physical parameters of stars, which are foundational for understanding the structure of stars and can verify stellar evolution theories (Singh & Deb 2011). EBs are used as a standard candle to determine the distances of various celestial bodies, including the Magellanic Clouds, M31, and M33 (Paczynski & Sasselov 1997; Guinan et al. 1998; Wytke & Wilson 2001; Bonanos et al. 2006). Studying EBs offers opportunities for searching for black holes and exoplanet candidates (Liu et al. 2024). In binary systems, when two components are close enough, material and energy transfer between the two components affects evolution, and these systems are called close binaries. Based on the geometrical structure of close binaries, Kopal (1955) classified them into three categories: detached binaries where neither component fills the Roche Lobe, semi-detached binaries where one component fills the Roche Lobe and

the other does not, and contact binaries where both components fill the Roche Lobe. Contact binaries are usually believed to form from detached binaries through angular momentum loss due to magnetic braking and gravitational radiation, and they may merge to form blue stragglers and FK Comae stars (Bradstreet & Guinan 1994; Qian et al. 2017, 2020; Liu et al. 2023).

Photometric and spectroscopic observations are important tools for determining physical parameters and analyzing the structure and evolution of EBs. Photometric light curves can be used to obtain physical parameters, such as photometric mass ratio, orbital inclination, relative radii, and luminosity ratio. Reliable photometric mass ratios can be obtained for semi-detached and contact binaries with the total eclipse minimum (Terrell & Wilson 2005; Li et al. 2021a). Additionally, the eclipsing times can be used to analyze orbital period variations, contributing to the study of dynamical evolution and searching for additional companions. Spectroscopic observations can be used to obtain the radial velocity curves, thereby precisely determining the mass ratio and mass function of EBs. Stellar spectra can also be used to derive atmospheric parameters, as well as to analyze chromospheric activity (Zhang et al. 2020; Li et al. 2021; Traven et al. 2020). The integrated analysis of photometric light curves and radial velocity curves enables the determination of accurate physical parameters of EBs, especially their absolute physical parameters (Feng et al. 2021).

The phenomenon of magnetic activity in binary systems has been frequently observed and studied (e.g., Strassmeier et al. 1988; Strassmeier et al. 1989; Long et al. 2021; Li et al. 2022; Yang & Wang 2024). This activity is triggered by the heating of the magnetic field in the outer atmosphere, which in turn leads to a variety of observable phenomena such as chromospheric activity, starspots, and activity cycles (Schrijver & Zwaan 2000). There are many spectral lines that can serve as indicators of chromospheric activity, including the Balmer series ( $H\alpha$ : 6562.8 Å,  $H\beta$ : 4861 Å,  $H\gamma$ : 4340.5 Å,  $H\delta$ : 4102 Å), the Ca II H & K lines (3968, 3933 Å), and the Ca II infrared triplet (IRT; 8498, 8542, 8662 Å). Among these, the  $H\alpha$  spectral line and the Ca II H & K lines, which are easily observable, are the most commonly utilized for studying chromospheric activity (Pavlenko et al. 2018; Zheng et al. 2021). Another phenomenon of magnetic activity that has been extensively studied is the O’Connell effect (O’Connell 1951), which has been observed on binaries (e.g., Qian et al. 2007; Li et al. 2014; Gao et al. 2021). O’Connell effect is manifested by that the two out-of-eclipse maxima of the light curves are not equal. In general, there are several explanations for the O’Connell effect: starspots due to magnetic activity (Binnendijk 1964), accretion of material between two components (Shaw 1994), circumstellar material around the binary (Liu & Yang 2003), and asymmetry of material due to the coriolis force (Zhou & Leung 1997), etc. Of these, starspots are considered as the most likely cause of the O’Connell effect (Qian et al. 2013; Li et al. 2016; Zhou et al. 2016).

We implemented a project called the “LAMOST Eclipsing Binaries Search (LEBS) Project”, which aims to search for and analyze EBs in the LAMOST Medium-Resolution Sky Survey field. This paper is the first work of our project, searching for and analyzing EBs around RA:  $23^h01^m51^s$ , Dec:  $+34^\circ36'45''$ . We selected this field as the target field because it has been observed 52 times by the LAMOST Medium-Resolution Survey DR9<sup>1</sup>. This provides an opportunity for obtaining a complete phase coverage of the radial velocity curve, and the spectra facilitate a comprehensive analysis of EBs. Section 2 describes observations and data reduction. Orbital parameters were determined in Section 3. Orbital period variations were analyzed in Section 4. In Section 5, the chromospheric activities of 13 binaries were analyzed using LAMOST medium-resolution spectra. Section 6 describes the discussions and conclusions.

## 2. OBSERVATIONS AND DATA REDUCTION

### 2.1. Photometry

#### 2.1.1. Ground-based photometric data

A 10 cm telescope at Xingming Observatory<sup>2</sup> was used to obtain photometric data. The telescope is equipped with an APOGEE U16M CCD, possessing  $4096 \times 4096$  square pixels and offering a field of view of  $239' \times 239'$ . During the observations, the filters of the Sloan  $r'$  and  $i'$  were used. The center of the telescope observed towards RA:  $23^h01^m51^s$ , Dec:  $+34^\circ36'45''$ . The exposure time for both filters was 120 seconds, the readout time was 40 seconds for each image, and the final cadence was 320 seconds because the two filters were observed alternately. The observations were conducted for 13 days, from September 2 to September 22, 2021. More than 900 valid images were collected for each filter, which were the ones after visual exclusion of those impacted by obvious poor weather conditions.

First, all observed CCD images were preprocessed, including bias subtraction, dark subtraction, and flat correction. The World Coordinate System information was acquired by matching the CCD frames with the Fourth U.S. Naval Observatory CCD

<sup>1</sup> <https://www.lamost.org/dr9/v1.0/>

<sup>2</sup> <http://xjltc.china-vo.org/>

Astrograph Catalog (UCAC4) using the *Xparallax viu*<sup>3</sup> software. We used the *Sep*<sup>4</sup> package to detect sources. *Photutils*<sup>5</sup> package was used for aperture photometry to obtain light curves for all sources in the field of view. 10 sources with strong and constant brightness were selected as reference stars. After determining the reference stars, we obtained differential light curves for all sources. Since there are no confirmed standard stars in the field of view, using the same method as Michel et al. (2019), we carried out the visual magnitude calibration of sources by subtracting the average of the observed magnitudes from the visual magnitudes of the 10 reference stars. We first chose sources with large standard deviations in the light curves as variable star candidates. Next, we manually excluded non-variable stars with spuriously large standard deviations, which may have been caused by the images that were not completely eliminated due to poor weather conditions, or by the stars located at the edge of the field and those contaminated by satellite crossings. Finally, we identified 53 variable stars, 48 are EBs and 5 are pulsating variables. The EBs we detected were renamed as LEBS-01 ~ LEBS-48. Among them, EBs with photometric data and LAMOST medium-resolution spectra were LEBS-01 ~ LEBS-13, and EBs with only photometric data were LEBS-14 ~ LEBS-48. By cross-matching with previously discovered EBs, we found that two EBs are newly discovered. The five pulsating variable stars have all been discovered previously, and the specific details of these stars are not discussed since it is beyond the scope of this paper. We used the period which provided by the The International Variable Star Index (VSX) website<sup>6</sup> for the 46 confirmed EBs. For 2 newly discovered targets, we used the Lomb-Scargle (LS) Periodograms (Zechmeister & Kürster 2009) to obtain their periods. The light curves were folded according to the corresponding period. The Gaussian Process (GP) method is widely used for time series analysis and is often used to model light curves and identify outliers in EBs (Aigrain & Foreman-Mackey 2023). We employed the GP method to fit the light curves and calculated the standard deviations ( $\sigma$ ) between the observed data and the GP model predictions. Data points with residuals exceeding  $3\sigma$  were considered as outliers, thereby yielding more accurate and reliable light curve models.

The phased light curves of 48 EBs and 5 pulsating variables are shown in Figure 1. The basic information of the 53 variable stars and the 10 reference stars are shown in Table 1.

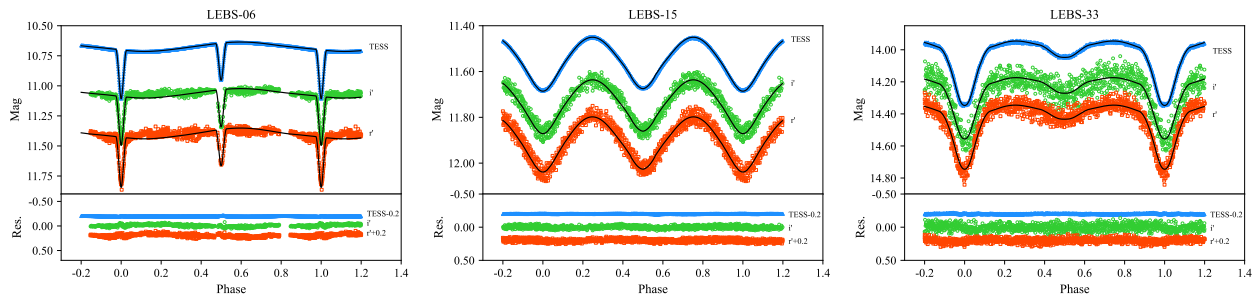


**Figure 1.** Light curves for the 53 variable stars. The colored symbols represent observational light curves, and the black lines represent theoretical light curves. The light curves of *TESS* have been shifted. The fitted residuals are displayed at the bottom of each panel. The complete figure in the online version of this article.

### 2.1.2. *TESS* observations

The *Transiting Exoplanet Survey Satellite* (*TESS*) is an all-sky survey that observes stars brighter than  $T_{mag} \approx 16$ , with a photometric precision from 60 ppm to 3 percent, enabling an array of exoplanet and stellar astrophysics investigations (Ricker et al. 2015; Oelkers & Stassun 2018). By cross-matching with the *TESS* data, we found that 50 of 53 variable stars were observed by *TESS* at 2 min cadence. We collected light curves from Mikulski Archive for Space Telescopes (MAST) but found that some targets are missing. Therefore, we carried out photometry for *TESS* to obtain light curves for all targets. We used the coordinates to search and download  $20 \times 20$  pixel *TESS* full-frame image (FFI) cut-outs (Brasseur et al. 2019) through the *lightkurve* package from the MAST archive (Lightkurve Collaboration et al. 2018). By using the thresholding method, apertures and background masks were created to generate light curves. Low-frequency trends were removed using Scipy’s Savitzky-Golay filter (Oliphant 2007). For LEBS-18, LEBS-21, LEBS-36, LEBS-37, LEBS-44, LEBS-45, and LEBS-48, we found that these targets were contaminated by the nearby stars due to the large pixel scale of *TESS* (21 arcsec), leading to diluted amplitudes. Although we

<sup>3</sup> <https://www.xparallax.com/>

<sup>4</sup> <https://sep.readthedocs.io/en/v1.1.x/>

<sup>5</sup> <https://photutils.readthedocs.io/en/stable/index.html>

<sup>6</sup> <https://www.aavso.org/vsx/index.php>

have removed the background light, the lightkurve package is currently unable to completely carry out the correction for the flux from other stars. For LEBS-37, we used the light curve provided by MAST, which completely corrects the contamination. For LEBS-18, LEBS-21, LEBS-36, LEBS-44, LEBS-45, and LEBS-48, since there are no light curves provided by MAST, we still used the light curves obtained through photometry with the lightkurve package. And for the other targets that are not contaminated by nearby stars, we used the light curves processed by lightkurve package, which were consistent with the those provided by MAST (if available). The light curves of the *TESS*-band are shown with blue symbols in Figure 1.

## 2.2. Spectroscopy

### 2.2.1. LAMOST Spectral Observations

LAMOST is a 4m reflecting Schmidt optical telescope at Xinglong Observatory, with a  $5^\circ$  field of view (Cui et al. 2012; Luo et al. 2015). The focal plane can accommodate up to 4000 optical fibers connected to 16 identical multi-objective optical spectrometers. LAMOST Low-Resolution Spectroscopic Survey (LRS) has a resolution of  $R \sim 1800$ , and the wavelength coverage is approximately 3700-9000Å. The Medium-Resolution Spectroscopic Survey (MRS) has a resolution of  $R \sim 7500$ . In the MRS mode, the wavelength coverage of the blue arm is 4950-5350 Å, and the coverage of the red arm is 6300-6800 Å (Yan et al. 2022). By cross-matching 48 EBs with LAMOST DR9, we obtained high-quality ( $S/N > 10$ ) medium-resolution spectra of 13 EBs (LEBS-01 ~ LEBS-13), which were used for subsequent analysis.

### 2.2.2. Radial velocity analysis

To avoid the influence of possible  $H\alpha$  emission line, only blue arm spectra were used to measure the radial velocities. Synthetic PHOENIX spectra (Husser et al. 2013) with reduced resolution to the same resolution as the LAMOST spectra ( $R \sim 7500$ ) were used as template spectra depending on the temperature (the calculation of temperatures of the two components is described in Section 3) of each EB. We used the cross-correlation function (CCF) method (Szalai et al. 2007; Matijević et al. 2010) to measure the radial velocities. The GaussPy+ package (Riener et al. 2019) was used to determine the peak position of the CCF curves. We used the method proposed by Zhang et al. (2021) for zero point correction of radial velocities. Rvfit code (Iglesias-Marzoa et al. 2015) was used to obtain the phased radial velocity curves, which are shown in Figure 2. The radial velocities of the 13 targets are listed in Table 2. As seen in Figure 2, the radial velocities of LEBS-12 and LEBS-13 show more scatter due to a limitation of the data, which were not used for orbital parameter study, and the results of the other 11 targets were used for subsequent orbital parameter analysis. For LEBS-03 and LEBS-08, radial velocity measurements were obtained at only three phases, which makes it difficult to obtain a unique solution. But in Section 3, by combing the radial velocity curves with the photometric light curves, we can obtain reliable orbital parameters, as the light curves provide crucial supplementary information. The large dispersion of LEBS-06 and LEBS-07 at phases 0 and 0.5 is due to poor data quality of the spectra. All 13 systems are all double-lined spectroscopic binaries, including LEBS-09, even though the primary component's luminosity accounts for more than 90% of the total (please refer to Section 3 for details), its CCF curve does indeed show double peaks near the phases of 0.25 and 0.75. Moreover, based on the formula  $m_2 - m_{total} = -2.5 \lg \frac{L_2}{L_{total}}$ ,  $m_{total} = 10.744$  (G-band) (Gaia Collaboration 2022),  $\frac{L_2}{L_{total}} = 0.093$  (*TESS*-band, which is very close to the G-band), we calculated the magnitude of the secondary component,  $m_2 = 13.352 (\pm 0.123)$ , which is within the observation limit of LAMOST ( $m \approx 15$ , G-band). Therefore, LEBS-09 is a double-lined spectroscopic binary.

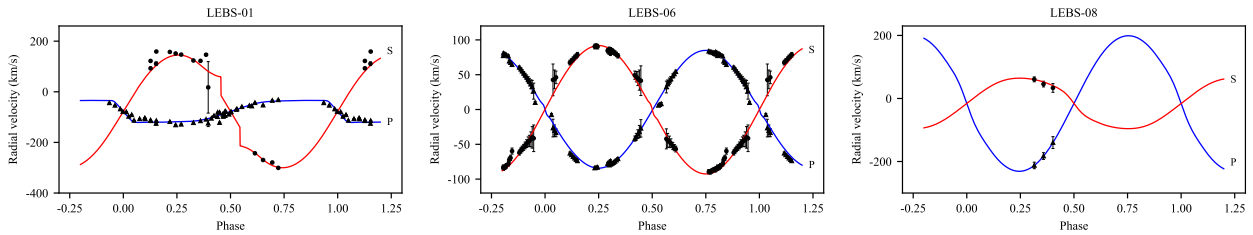


**Figure 2.** Theoretical and observational radial velocity curves of 13 targets. The blue lines show the theoretical curves of the primary components, and the red lines show the theoretical curves of the secondary components. The complete figure in the online version of this article.

## 3. ORBITAL PARAMETERS

The 2015 version of W-D code (Wilson & Devinney 1971; Wilson 1979, 1990) was used to determine the orbital parameters of 48 EBs. When setting parameters, the calculation rules for the temperatures of the primary and secondary components are as

**Table 1.** Basic information for 53 variable stars and the 10 reference stars.

Name(This paper)	Name(VSX website)	$\alpha_{2000}$	$\delta_{2000}$	Period(d)	$T_{eff}(K)$
LEBS-01	V0663 Peg	22:52:59.60	+33:54:26.4	0.6244506	6830( $\pm$ 25)
LEBS-02	ATO J343.6450+34.6956	22:54:35.00	+34:41:44.3	1.13162	6776( $\pm$ 41)
LEBS-03	ASASSN-V J225551.75+331017.3	22:55:51.75	+33:10:17.3	2.39499	5744( $\pm$ 22)
LEBS-04	V0404Peg	22:56:30.90	+33:55:12.1	0.419195	6400( $\pm$ 71)
LEBS-05	V0751 Peg	22:58:40.48	+34:37:46.3	0.60763649	6765( $\pm$ 13)
LEBS-06	V0557 Peg	22:59:23.53	+32:51:33.4	2.3845	4991( $\pm$ 93)
LEBS-07	ASASSN-V J230252.69+342300.6	23:02:52.61	+34:23:00.5	0.60097	6710( $\pm$ 23)
LEBS-08	V0593 And	23:03:44.07	+36:15:22.9	0.372177	5635( $\pm$ 66)
LEBS-09	ER Peg	23:05:46.80	+33:29:07.1	2.27467	7749( $\pm$ 62)
LEBS-10	V0568 Peg	23:08:13.01	+33:03:03.8	0.247074	4256( $\pm$ 44)
LEBS-11	ASASSN-V J231002.29+342823.4	23:10:02.23	+34:28:23.2	0.433999	6523( $\pm$ 22)
LEBS-12	V0747 Peg	22:55:49.91	+34:01:12.0	0.51431	7153( $\pm$ 54)
LEBS-13	V0579 And	22:59:11.09	+36:21:17.8	0.338134	5538( $\pm$ 21)
LEBS-14	V0478 Lac	22:50:47.74	+35:40:56.2	0.445665	6230( $\pm$ 98)
LEBS-15	V0548 Peg	22:51:34.19	+34:57:53.0	0.38162	6590( $\pm$ 64)
LEBS-16	ASASSN-V J225203.51+325424.4	22:52:03.57	+32:54:25.4	0.318274	5877( $\pm$ 44)
LEBS-17(new)	—	22:52:23.27	+33:19:21.1	16.94967	5757( $\pm$ 84)
LEBS-18	ASASSN-V J225235.00+362014.1	22:52:35.00	+36:20:14.2	1.0859832	7220( $\pm$ 54)
LEBS-19	BD+34 4783	22:52:50.63	+35:31:58.8	4.118	6426( $\pm$ 64)
LEBS-20	V0479 Lac	22:52:50.69	+35:58:56.5	0.34575	5760( $\pm$ 33)
LEBS-21	ASASSN-V J225325.14+354532.5	22:53:25.24	+35:45:32.8	0.354248	5380( $\pm$ 100)
LEBS-22	V0664Peg	22:53:59.34	+33:33:46.8	0.40037	6770( $\pm$ 76)
LEBS-23	ASASSN-V J225402.95+324527.6	22:54:02.95	+32:45:27.6	0.267356	4520( $\pm$ 81)
LEBS-24	ASASSN-V J225412.47+335322.7	22:54:12.50	+33:53:24.1	0.331146	5933( $\pm$ 19)
LEBS-25	ASASSN-V J225440.29+362222.9	22:54:40.40	+36:22:22.3	0.436834	6840( $\pm$ 73)
LEBS-26	VW Peg	22:56:23.58	+33:13:43.8	21.071749	5630( $\pm$ 35)
LEBS-27	ASASSN-V J225650.69+345101.6	22:56:50.70	+34:51:01.9	0.33193	5930( $\pm$ 33)
LEBS-28	V0749 Peg	22:57:19.54	+34:27:58.2	0.4167682	6657( $\pm$ 47)
LEBS-29	ASASSN-V J225721.72+350704.5	22:57:21.87	+35:07:03.1	5.1010937	6707( $\pm$ 66)
LEBS-30	ASASSN-V J225822.44+341230.9	22:58:22.46	+34:12:31.9	1.62663	7340( $\pm$ 137)
LEBS-31	ASASSN-V J225837.15+333030.0	22:58:37.15	+33:30:30.0	0.255738	5543( $\pm$ 28)
LEBS-32(new)	—	22:59:12.60	+33:30:15.0	1.00608444	4990( $\pm$ 164)
LEBS-33	ASASSN-V J230021.29+333532.7	23:00:21.24	+33:35:32.0	0.53253	6417( $\pm$ 54)
LEBS-34	V0667 Peg	23:03:06.37	+33:51:51.2	0.3933915	6303( $\pm$ 40)
LEBS-35	ASASSN-V J230313.97+344622.3	23:03:13.83	+34:46:21.9	0.4228617	4043( $\pm$ 41)
LEBS-36	ASASSN-V J230358.08+335926.6	23:03:57.99	+33:59:27.4	1.86598	7330( $\pm$ 93)
LEBS-37	ASASSN-V J230416.79+360511.9	23:04:16.79	+36:05:11.9	3.52444	6723( $\pm$ 97)
LEBS-38	ASASSN-V J230437.49+344949.5	23:04:37.38	+34:49:49.7	0.2901	5273( $\pm$ 50)
LEBS-39	ASASSN-V J230506.67+325332.8	23:05:06.57	+32:53:32.8	0.390655	6187( $\pm$ 106)
LEBS-40	ASASSN-V J230607.98+341038.9	23:06:08.01	+34:10:39.0	0.376725	6097( $\pm$ 68)
LEBS-41	V0669 Peg	23:06:28.11	+33:40:09.6	0.3970365	5843( $\pm$ 60)
LEBS-42	ASASSN-V J230635.23+325632.1	23:06:35.16	+32:56:32.0	0.2669558	5060( $\pm$ 109)
LEBS-43	ASASSN-V J230722.65+360358.1	23:07:22.67	+36:03:58.1	0.2495618	4933( $\pm$ 136)
LEBS-44	ASASSN-V J230819.40+350853.0	23:08:19.42	+35:08:53.2	0.874223	4830( $\pm$ 10)
LEBS-45	ASASSN-V J230835.43+354143.9	23:08:35.33	+35:41:43.6	0.299564	5100( $\pm$ 10)
LEBS-46	CSS_J230837.7+333905	23:08:37.76	+33:39:05.5	0.389588	6400( $\pm$ 110)
LEBS-47	CSS_J230838.3+334753	23:08:38.34	+33:47:53.0	0.8839762	6601( $\pm$ 33)
LEBS-48	ASASSN-V J230923.71+361629.8	23:09:23.71	+36:16:30.1	0.314522	5377( $\pm$ 50)
Pulsatingvariablestar	CSS_J225208.2+355354	22:52:08.20	+35:53:54.8	0.7324429	—
Pulsatingvariablestar	CSS_J225940.9+325805	22:59:40.90	+32:58:05.1	0.6087498	—
Pulsatingvariablestar	CSS_J230156.0+360059	23:01:56.00	+36:00:59.7	0.5083755	—
Pulsatingvariablestar	V0564 Peg	23:03:10.27	+34:25:07.1	0.318785	—
Pulsatingvariablestar	CSS_J230536.3+344154	23:05:36.42	+34:41:54.1	0.198771	—
Comparison star	—	23:06:49.00	+36:09:01.3	—	—
Check star	—	22:57:21.57	+35:22:00.64	—	—
Check star	—	22:57:23.03	+35:25:00.00	—	—
Check star	—	22:58:17.74	+33:30:27.25	—	—
Check star	—	22:58:26.06	+33:29:18.85	—	—
Check star	—	23:04:53.39	+36:08:37.18	—	—
Check star	—	23:05:49.00	+33:00:46.7	—	—
Check star	—	23:05:50.03	+33:05:03.29	—	—
Check star	—	23:06:49.07	+36:09:01.26	—	—
Check star	—	23:06:57.53	+36:09:55.56	—	—
Check star	—	23:06:58.00	+36:09:55.5	—	—
Check star	—	23:06:58.86	+34:52:05.79	—	—

"Name(This paper)" represents the name used in this paper. "Name(VSX website)" represents the name on the VSX website. " $\alpha_{2000}$ " and " $\delta_{2000}$ " represent the right ascension and declination of EBs, respectively. "Period(d)" represents the orbital period for EBs and the pulsation period for pulsating variable stars, the periods for LEBS-02, LEBS-17, and LEBS-32 are derived from the Lomb-Scargle method, while the rest are obtained through queries on the VSX website. " $T_{eff}(K)$ " represents the effective temperature of the EBs, those for LEBS-01 to LEBS-13 are from the LAMOST spectra, and for LEBS-14 to LEBS-48 are determined using the de-reddened color index.

**Table 2.** The radial velocity values of 13 EBs.

LEBS-01	HJD	phase	RV-P(km/s)	Error(km/s)	RV-S(km/s)	Error(km/s)
	2458408.03318	0.100	-103.67	0.90	-	-
	2458408.04951	0.127	-114.60	1.07	92.76	4.29
	2458408.06645	0.153	-125.41	1.57	110.90	7.26
	2458408.10554	0.217	-118.35	0.72	157.43	1.68
	2458408.12299	0.244	-131.21	0.99	151.36	2.52
	2458408.13932	0.270	-128.59	1.39	146.98	3.25
	2458410.06862	0.360	-115.08	0.88	122.21	2.28
	2458410.08485	0.386	-108.95	0.69	146.48	3.23
	2458416.09653	0.014	-79.78	0.86	-	-
	2458416.11276	0.039	-90.99	0.80	-	-
	2458446.93441	0.396	-124.60	12.84	17.55	101.74
	2458447.95055	0.025	-97.44	0.70	-	-

“HJD” represents the observation time. “Phase” represents the phase used in this work, which is determined based on the ephemeris calculated in our work. “RV-P(km/s)” and “RV-S(km/s)” represent the radial velocity of the primary and secondary components, respectively.

This table is available in its entirety in machine-readable form through China VO (<https://nadc.china-vo.org/res/r101429/>).

follows. Firstly, the temperature of the primary components are estimated: (1) For the targets with LAMOST spectra, we used the LAMP temperatures (Wu et al. 2011) given by LAMOST spectra. Considering the wavelength coverage of the low-resolution spectra was wider than that of the medium-resolution spectra, we first used the temperatures given by the low-resolution spectra. For targets with only medium-resolution spectra, we used the temperatures from the medium-resolution spectra. The average value was taken as the final temperature if the target has multiple temperatures.(2) For the targets without LAMOST spectra, we used the dereddening color index, considering 3D extinction (Green et al. 2019). Based on the magnitudes of B, V, g, r bands from AAVSO Photometric All Sky Survey (Henden et al. 2015) and J, K bands from 2MASS (Cutri et al. 2003), we calculated B-V, g-r, J-K. According to the relationship between color index and temperature (Pecaut & Mamajek 2013), three temperatures were obtained, and we adopted the average temperature as the final temperature. However, the temperatures estimated by the LAMP or color index are actually the average values of the two components. Therefore, these values were initially set as the temperature of the primaries; when we have obtained the temperature ratio,  $T_{2i}/T_{1i}$ , and the radius ratio,  $k = r_2/r_1$ , through the convergent solution of the W-D code, the more accurate temperature of each component ( $T_{1c}$ ,  $T_{2c}$ ) can be calculated using the following equations (Zwitter et al. 2003; Christophoulou & Papageorgiou 2013):

$$T_{1c} = \left( \frac{(1 + k^2)T_{1i}^4}{1 + k^2\left(\frac{T_{2i}}{T_{1i}}\right)^4} \right)^{0.25}, \quad (1)$$

$$T_{2c} = T_{1c} \frac{T_{2i}}{T_{1i}}. \quad (2)$$

Particularly, the temperatures obtained through the LAMOST spectra and determined using the color index are not exactly corresponding to quadrature (which is assumed in the above equations), but slightly differ from the temperatures corresponding to quadrature. Although we cannot obtain exact temperatures that correspond to quadrature, we try to use these temperatures from LAMOST spectra or color index as initial values, and then calculate the more accurate temperatures of the two components based on Equation 1 and 2. Then,  $T_{1c}$  and  $T_{2c}$  were set as initial values, with the primary temperature set as a fixed parameter and the secondary temperature as an adjustable one. Recalculations were made using the W-D code, the convergent solutions obtained are listed in Table 3.

The gravity darkening and bolometric albedo coefficients were set to  $g = 0.32$  and  $A = 0.5$  for a convective atmosphere ( $T_{eff} < 7200$  K), and  $g = 1$  and  $A = 1$  for a radiative atmosphere ( $T_{eff} > 7200$  K) (von Zeipel 1924; Lucy 1967; Ruciński 1969). The limb darkening and the bolometric coefficients of the two components were determined according to the table of van Hamme (1993). We set the mode based on the different characteristics of each eclipsing binary: Mode 2 (for detached system), Mode 3 (for overcontact system), Mode 4 (for semi-detached system with the more massive one filling its Roche lobe), and Mode 5 (for semi-detached system with the less massive star filling its Roche lobe).

The mass ratio ( $q$ ) plays an important role in studying the Roche-geometry and physical properties of EBs (Jatmiko et al. 2019; Guo et al. 2020). For the 11 targets with both light curves and radial velocity curves, we could obtain accurate mass ratios and determine absolute physical parameters by W-D code. The initial mass ratios obtained from the fitting of rvfit code. For the 37 targets with only light curves, the rules for the initial mass ratios were as follows: (1) For the detached binaries, the mass

ratios are insensitive to the light curves (Wyithe & Wilson 2001; Terrell & Wilson 2005), so we adopted the method provided by Kjurkchieva & Vasileva (2018) to estimate their initial mass ratios. Assuming that the components of the EBs are main-sequence stars and the primary temperature  $T_1^i = T_{eff}$ , the temperature of the secondary component can be estimated as  $T_2^i = T_1^i (\frac{d_2}{d_1})^{0.25}$ , where  $d_1$  and  $d_2$  are the depths of the eclipses in relative flux. Then, the mass ratios of detached binaries are  $q = (\frac{T_2^i}{T_1^i})^{1.6}$ . (2) For semi-detached and contact binaries, the initial mass ratios were determined by the q-search method. We carried out calculations over a series of q-values, ranging from 0.1 to 10.0 with a step of 0.1. For each assumed q-value, a convergent solution and mean residuals were obtained. We treated the q-value corresponding to the smallest mean residuals as the initial mass ratio of the system. The q-search method is widely used to determine mass ratios of binaries when radial velocity curves are not required (Niarchos et al. 1997; Özdemir et al. 2003; Caton et al. 2019; Sun et al. 2020).

**Table 3.** Orbital parameters of 48 EBs from W-D solutions.

Parameters	LEBS-01	LEBS-02	LEBS-03	LEBS-04	LEBS-05
Mode	3	3	2	3	3
$T_1$ (K)	6972(±30)	6862(±44)	5813(±32)	6426(±84)	6884(±16)
$T_2$ (K)	6183(±57)	6604(±123)	5688(±57)	6292(±161)	6193(±32)
$i$ (°)	89.058(±0.158)	36.541(±0.239)	89.248(±0.090)	61.645(±0.088)	69.527(±0.083)
$q(M_2/M_1)$	0.220(±0.001)	0.632(±0.004)	2.210(±0.020)	0.214(±0.002)	0.190(±0.001)
$\Omega_1$	2.242(±0.003)	3.071(±0.015)	8.843(±0.026)	2.211(±0.006)	2.180(±0.002)
$\Omega_2$	2.242(±0.003)	3.071(±0.015)	13.250(±0.105)	2.211(±0.006)	2.180(±0.002)
$\Omega_{in}$	2.282	3.132	5.547	2.267	2.207
$\Omega_{out}$	2.143	2.762	4.943	2.131	2.085
$f(f_1)$ (%)	29.2(±2.1)	11.0(±6.4)	62.7(±0.2)	41.0(±4.4)	22.2(±1.7)
$f_2$ (%)	—	—	41.9(±0.3)	—	—
$r_1$	0.527(±0.001)	0.431(±0.003)	0.152(±0.000)	0.536(±0.001)	0.534(±0.000)
$r_2$	0.271(±0.003)	0.320(±0.008)	0.172(±0.001)	0.269(±0.007)	0.263(±0.003)
$L_{1r}/L_r$	0.856(±0.001)	0.640(±0.005)	0.458(±0.001)	0.806(±0.002)	0.867(±0.001)
$L_{1i}/L_i$	0.846(±0.001)	0.633(±0.005)	0.455(±0.001)	0.804(±0.002)	0.859(±0.001)
$L_{1l}/L_l$	0.847(±0.001)	0.634(±0.005)	0.455(±0.001)	0.804(±0.002)	0.860(±0.001)
Latitude (star1)	0.571	1.598	—	—	—
Longitude (star1)	0.478	2.389	—	—	—
Radius (star1)	0.257	0.330	—	—	—
$T_s$ (star1)	0.880	1.202	—	—	—
$V_\gamma$ (km/s)	-78.570(±1.293)	-11.990(±2.300)	-59.700(±5.199)	-16.810(±2.064)	-57.810(±0.667)
$a(R_\odot)$	3.524(±0.103)	7.399(±0.417)	9.306(±0.444)	2.509(±0.077)	3.264(±0.042)

“Mode” represents the configuration mode of EBs, where “2” denotes a detached system, “3” denotes an overcontact system, “4” denotes a semi-detached system with the more massive star filling its Roche Lobe, and “5” denotes a semi-detached system with the less massive star filling its Roche Lobe. “ $T_1$ (K)” and “ $T_2$ (K)” represent the temperature of the primary and secondary components, respectively. “ $i$ (°)” represents the orbital inclination. “ $q(M_2/M_1)$ ” represents the mass ratio. “ $\Omega_1$ ” and “ $\Omega_2$ ” represent the dimensionless potential energy of the primary and secondary components, respectively. “ $\Omega_{in}$ ” and “ $\Omega_{out}$ ” represent the potential energy of the inner critical surface and the outer critical surface, respectively. “ $f$ (%)” represents the contact degree for contact binaries. “ $f_1$ (%)” and “ $f_2$ (%)” represent the fill-out factor of the primary and secondary components for detached and semi-detached binaries. “ $r_1$ ” and “ $r_2$ ” represent the relative radius of the primary and secondary components, which are their radii relative to the semi-major axis, respectively. “ $L_{1r}/L_r$ ”, “ $L_{1i}/L_i$ ” and “ $L_{1l}/L_l$ ” represent the share of the primary component’s luminosity in the Sloan r’, Sloan i’ and *TESS* bands, respectively. “ $L_{3r}/L_r$ ”, “ $L_{3i}/L_i$ ” and “ $L_{3l}/L_l$ ” represent the share of the third light’s luminosity in the Sloan r’, Sloan i’ and *TESS* bands, respectively. “Latitude”, “Longitude”, “Radius” and “ $T_s$ ” represent the latitude, longitude, angular radius and temperature factor of the starspots, respectively. “ $V_\gamma$  (km/s)” represents the radial velocity of the system. “ $a(R_\odot)$ ” represents the semi-major axis. “e” represents eccentricity. “ $\omega$ ” represents the periastron angle. “-” indicates the corresponding parameter can’t be obtained for the EBs.

This table is available in its entirety in machine-readable form through China VO (<https://nadc.china-vo.org/res/r101429/>).

In the process of solving the orbital parameters, there are several special types of targets, for which the analysis was as follows: (1) For LEBS-18, LEBS-21, LEBS-36, LEBS-37, LEBS-44, LEBS-45, LEBS-48, the amplitudes of the *TESS*-band light curves were diluted due to the contamination of nearby stars resulting from the large pixel scale (21 arcsec) of *TESS*. The third light would make the photometric solution complex and uncertain (Rucinski 2010). We first estimated the physical parameters through the Sloan r’ and i’ bands. Then, we used these physical parameters and set the third light to be adjustable for the *TESS* band to

determine the third light. Next, we set the third light of the *TESS* band to non-adjustable, and the final solutions were determined by analyzing the light curves of the three bands. (2) For LEBS-01, LEBS-02, LEBS-06, LEBS-08, LEBS-10, LEBS-14, LEBS-20, LEBS-22, and LEBS-40, the two maxima of the light curves showed asymmetric characteristics. This phenomenon is the so-called "O'Connell effect" (O'Connell 1951). We added starspots on one or both components to address that. (3) For the three detached binaries, LEBS-17, LEBS-26, and LEBS-29, the light curves showed that the orbits have apparent eccentricity. Eccentricity  $e$  and periastron angle  $\omega$  were calculated by the following equations (Kjurkchieva & Vasileva 2015),

$$e_0 \cos \omega_0 = \frac{\pi}{2} [(\varphi_2 - \varphi_1) - 0.5], \quad (3)$$

$$e_0 \sin \omega_0 = \frac{w_2 - w_1}{w_2 + w_1}, \quad (4)$$

where  $\varphi_{1,2}$  are the phase of primary and secondary minima, and  $w_{1,2}$  are the widths of them.

The orbital parameters from the W-D solutions are listed in Table 3. The orbital parameter solutions for total eclipse contact and semi-detached binaries, as well as for systems with radial velocity curves, are uniquely determined (including LEBS-01 to LEBS-11, LEBS-21, LEBS-22, LEBS-28, LEBS-34, LEBS-41, and LEBS-48). The solutions for other systems are not unique; the solutions presented in Table 3 are the optimal solutions (including LEBS-12 to LEBS-20, LEBS-23 to LEBS-27, LEBS-29 to LEBS-33, LEBS-35 to LEBS-40, and LEBS-42 to LEBS-47). The uncertainties in the orbital parameters are fitting errors, which are generally underestimated (Prša & Zwitter 2005). Some errors are reported as 0.000, which are attributed to rounding effects. The theoretical light curves (black lines) and the fitting residuals are shown in Figure 1. The theoretical radial velocity curves (blue and red lines represent primary and secondary components, respectively) considering proximity effect are shown in Figure 2.

#### 4. ORBITAL PERIOD INVESTIGATIONS

Studying orbital period variations promotes the research of dynamic interactions of binary systems, searching for third bodies, and material transfer between two components of binary systems (Zhou et al. 2016; Li & Qian 2013; Pi et al. 2019). For the 26 targets with sufficient eclipsing times, we calculated the O-C (observed eclipsing minimum minus calculated eclipsing minimum) values to analyze their orbital period variations. We recorded the eclipsing minima from the O-C gateway<sup>7</sup> and previous studies, collected many photometric survey light curves and then used the K-W method (Kwee & van Woerden 1956) to calculate the minima, including the following surveys: the All-Sky Automated Survey for SuperNovae (ASAS-SN, Shappee et al. 2014; Kochanek et al. 2017; Jayasinghe et al. 2018), the Zwicky Transient Facility (ZTF) survey (Bellm et al. 2019; Masci et al. 2019), Wide Angle Search for Planets (WASP, Butters et al. 2010). We also used data from the American Association of Variable Star Observers (AAVSO, Henden et al. 2016). Since the ASAS-SN and ZTF observations were discrete, we used the Li method (Li et al. 2020) to group and fold the data into one period and then calculate the minima. We used the online tool<sup>8</sup> to convert HJD to BJD for all surveys uniformly. The time standard of the BJD values is TDB. All minima, errors, and their sources are listed in Table 4.

We calculated the O-C values according to the following equation,

$$BJD = BJD_0 + P \times E, \quad (5)$$

where  $E$  represents the cycle number. The O-C values of 26 targets are plotted in Figure 3, among which the O-C curves of 16 targets exhibit a parabolic trend, 8 targets show a linear trend, and 2 targets (LEBS-14 and LEBS-41) display periodic variations. The fitting parameters of O-C curves followed Equation 6 except for LEBS-14 and LEBS-41,

$$O - C = \Delta T_0 + \Delta P_0 \times E + \frac{\beta}{2} \times E^2, \quad (6)$$

where  $\Delta T_0$  and  $\Delta P_0$  represent the corrections of the initial epoch and the orbital period,  $\beta$  represents the long-term changing rate of the orbital period. For LEBS-14 and LEBS-41, the O - C curves showed periodic variations, so the fitting parameters followed Equation 7,

$$O - C = \Delta T_0 + \Delta P_0 \times E + A \times \sin\left(\frac{2\pi}{P_{mod}} \times E + \varphi\right), \quad (7)$$

<sup>7</sup> <http://var2.astro.cz/ocgate/>

<sup>8</sup> <https://astroutils.astronomy.osu.edu/time/hjd2bjd.html>



**Table 4.** The eclipsing times of 26 EBs.

LEBS-01	BJD	Error	Epoch	O-C	Residuals	Source	BJD	Error	Epoch	O-C	Residuals	Source
	2453226.57889	0.00188	-10567.5	-0.01869	-0.00376	(1)	2454022.44175	0.00242	-9293	-0.01812	-0.00496	(1)
	2453227.52106	0.00168	-10566	-0.01320	0.00173	(1)	2454057.41571	0.00189	-9237	-0.01340	-0.00031	(1)
	2453232.51913	0.00207	-10558	-0.01074	0.00419	(1)	2454295.64458	0.00206	-8855.5	-0.01243	0.00013	(1)
	2453237.51414	0.00196	-10550	-0.01133	0.00358	(1)	2454295.64476	0.00205	-8855.5	-0.01225	0.00031	(1)
	2453242.50841	0.00195	-10542	-0.01266	0.00224	(1)	2454319.68582	0.00147	-8817	-0.01254	-0.00004	(1)
	2453256.55131	0.00243	-10519.5	-0.01990	-0.00503	(1)	2454326.55438	0.00113	-8806	-0.01294	-0.00045	(1)
	2453262.48550	0.00131	-10510	-0.01799	-0.00314	(1)	2454329.67743	0.00102	-8801	-0.01214	0.00034	(1)
	2453265.61234	0.00168	-10505	-0.01341	0.00144	(1)	2454330.61769	0.00214	-8799.5	-0.00856	0.00392	(1)
	2453271.54323	0.00228	-10495.5	-0.01480	0.00004	(1)	2454331.55086	0.00125	-8798	-0.01206	0.00042	(1)
	2453950.63662	0.00112	-9408	-0.01144	0.00189	(1)	2454334.67625	0.00105	-8793	-0.00892	0.00355	(1)
	2453970.61679	0.00133	-9376	-0.01368	-0.00040	(1)	2454350.59320	0.00142	-8767.5	-0.01546	-0.00303	(1)
	2453980.60857	0.00122	-9360	-0.01311	0.00014	(1)	2454351.53394	0.00120	-8766	-0.01140	0.00103	(1)
	2453990.60279	0.00241	-9344	-0.01010	0.00313	(1)	2454355.58875	0.00176	-8759.5	-0.01552	-0.00309	(1)
	2453997.46588	0.00111	-9333	-0.01597	-0.00275	(1)	2454360.58175	0.00221	-8751.5	-0.01812	-0.00571	(1)
	2454005.58144	0.00218	-9320	-0.01827	-0.00506	(1)	2454361.52335	0.00119	-8750	-0.01320	-0.00079	(1)

"BJD" represents the observed eclipsing minima times. "Epoch" represents the cycle number. "O-C" and "Residuals" represent the observed minima minus calculated minima and the corresponding fitting residuals, respectively. "Source" represents the source of the observed minima. (1) WASP; (2)AAVSO; (3)ASAS-SN; (4)O-C Gateway; (5)Other paper; (6)ZTF; (7)This paper; (8)TESS

This table is available in its entirety in machine-readable form through China VO (<https://nadc.china-vo.org/res/r101429/>).

where  $A$ ,  $P_{mod}$ , and  $\varphi$  represent the quasi-sinusoidal change's amplitude, period, and initial phase. The fitting parameters of 26 targets were calculated as shown in Table 5.

There are special explanations for some targets. (1) Due to the incorrect period, the O-C curves of LEBS-04, LEBS-10, LEBS-20, and LEBS-22 showed trends in multiple segments. We selected the most prominent trend to correct the period and recalculate the O-C values using the corrected period. This method has been addressed in many studies, such as Li et al. (2020). (2) Due to the eccentric orbits, the O-C values of the primary and secondary minima of LEBS-26 and LEBS-29 could not be fitted with a single line. Both the primary and secondary minima of LEBS-29 showed a linear trend with slopes less than zero. The primary minima of LEBS-26 showed a linear trend with slopes more than zero, and the secondary components showed less than zero, which was the effect of the apsidal motion (Sterne 1939).

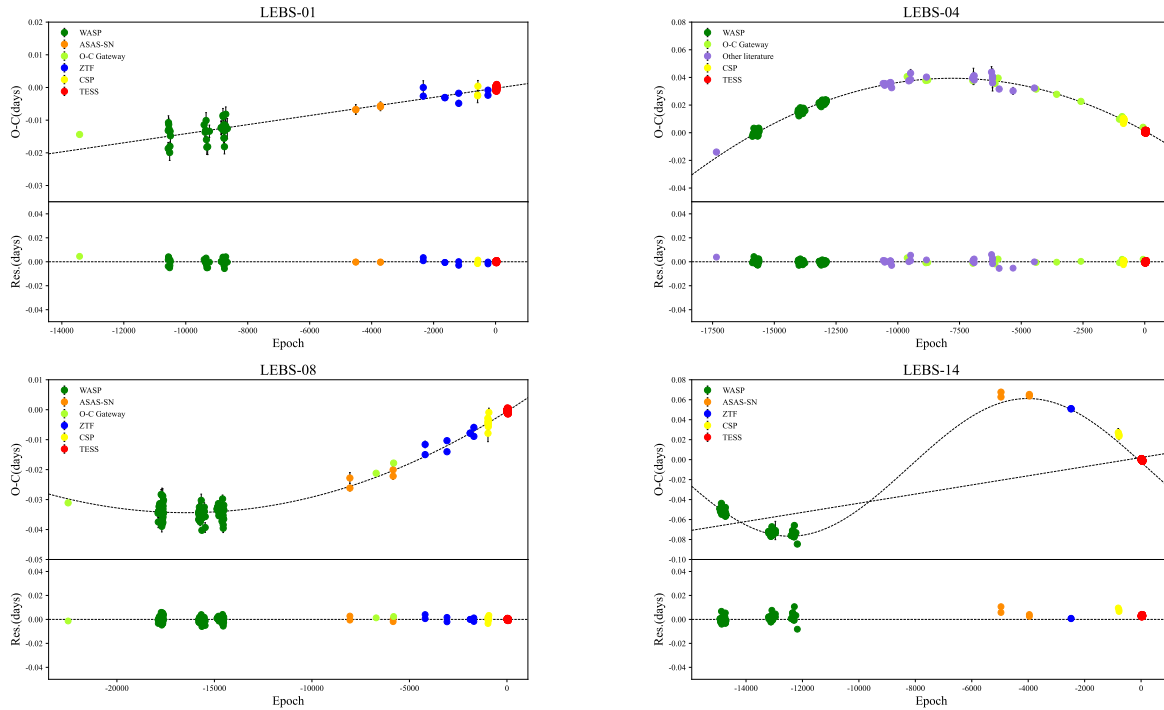


**Figure 3.** The O-C curves of 26 EBs. The O-C values and the fitting curves are shown at the top panels, and the residuals are at the bottom. The complete figure in the online version of this article.

## 5. CHROMOSPHERIC ACTIVITY INVESTIGATIONS

Chromospheric activity can influence material and energy transfer in binary systems, potentially affecting their evolution (Mityan et al. 2020). Therefore, the study of chromospheric activity in EBs is of great significance for revealing the mechanisms of internal energy release in stars, understanding the structural changes during the process of stellar evolution, and verifying the theories of stellar evolution (Fang et al. 2018). We analyzed the  $H\alpha$  (6562.5Å) emission line, whose equivalent width (EW) can effectively reflect the stellar chromospheric activity level (Hall 2008). Due to the influence of the photospheric layer, it was difficult to observe  $H\alpha$  emission lines directly. Therefore, the chromospheric emission lines were estimated by subtracting the photospheric contribution from the system spectra (Barden 1985). We analyzed chromospheric activity for the 13 targets with LAMOST medium-resolution spectra as follows:

- (1) Selected two templates and downloaded the spectra. The templates were selected from the inactive star catalog from Zhang et al. (2021). The temperature difference between the two templates and the two components of the target was less than 100 K.
- (2) Normalized the target and template spectra and removed the cosmic rays.
- (3) Generated synthetic spectra. We used the FORTRAN code STARMOD developed by Barden (1985), which was used by many researchers (e.g. Montes et al. 2000; López-Santiago et al. 2010; Panchal et al. 2022). The program synthesized the spectra by treating the two nonactive template spectra as the primary and secondary components, respectively, and took into account the effects of rotation, radial velocity, and the luminosity ratio. We initially assumed synchronous rotation, the rotation speed was estimated to be used as an input value for STARMOD, and then STARMOD fits the spectra to obtain the best results.
- (4) Obtained the subtracted spectra by subtracting the synthesized spectra from the target spectra. Gaussian fit was performed on the  $H\alpha$  emission lines of the subtraction spectra to calculate equivalent width (EW).

The observed, synthetic, and subtracted spectra are shown in Figure 4. The values of EW are shown in Table 2. The distribution of the EW versus phases are shown in Figure 5.

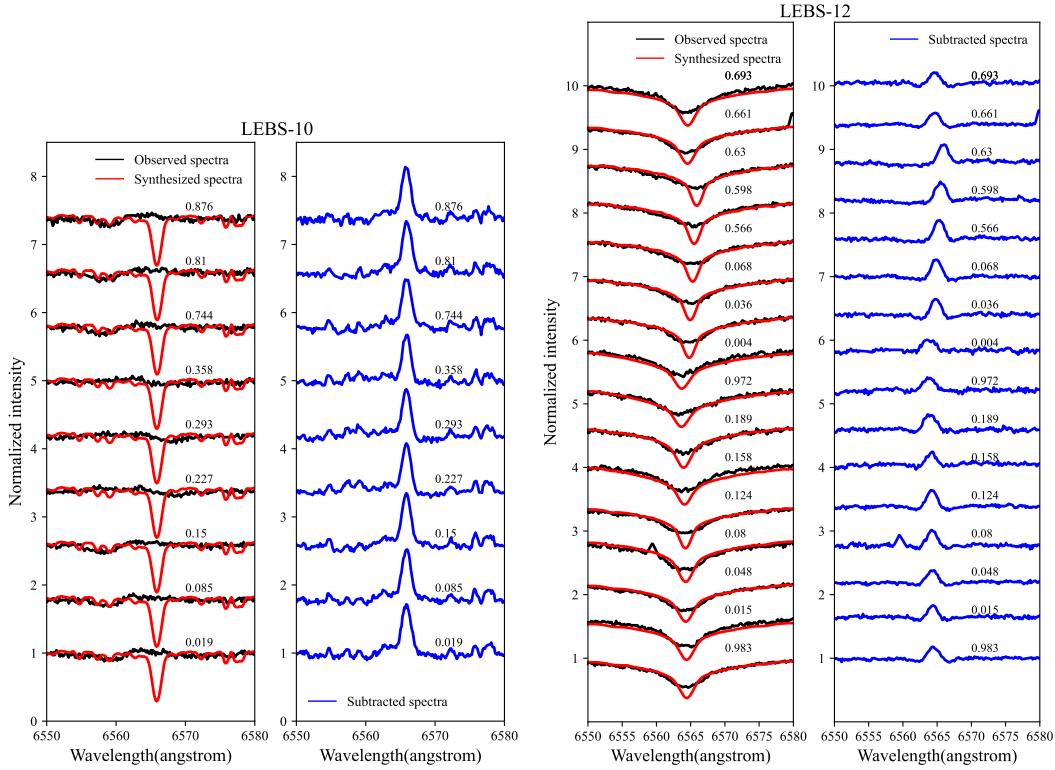


**Figure 4.** Observed, synthetic, and subtracted spectra from LAMOST medium-resolution for 13 EBs. The complete figure in the online version of this article.

## 6. DISCUSSTIONS AND CONCLUSIONS

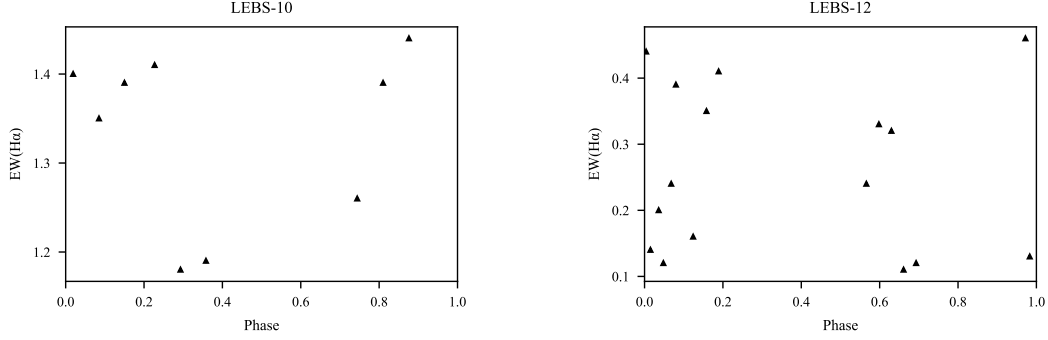


**Figure 5.** Distribution of equivalent widths (EW) of H $\alpha$  emission lines versus phases for 13 EBs. The complete figure in the online version of this article.

**Table 5.** The fitting parameters based on the O-C analysis and the material transfer parameters.

Target	$P_C$ (days)	$T_C$ (days)	$\beta$ (d/yr)	$dM_1/dt$ ( $M_\odot$ /yr)	$\tau$ (yr)	$\tau_{th}$ (yr)
LEBS-01	0.6244520( $\pm 3.00 \times 10^{-8}$ )	2459825.47905( $\pm 0.00016$ )	—	—	—	—
LEBS-03	2.3950521( $\pm 5.60 \times 10^{-7}$ )	2459825.66295( $\pm 0.00062$ )	—	—	—	—
LEBS-04	0.4191665( $\pm 5.61 \times 10^{-8}$ )	2459825.70845( $\pm 0.00011$ )	$-1.26(\pm 0.00) \times 10^{-9}$	$-2.35 \times 10^{-7}$	$4.22 \times 10^6$	$3.56 \times 10^6$
LEBS-05	0.6076468( $\pm 3.04 \times 10^{-7}$ )	2459825.41955( $\pm 0.00028$ )	$9.06(\pm 0.60) \times 10^{-10}$	$7.42 \times 10^{-8}$	—	—
LEBS-06	2.3843446( $\pm 7.65 \times 10^{-7}$ )	2459825.37521( $\pm 0.00091$ )	—	—	—	—
LEBS-07	0.6009719( $\pm 1.71 \times 10^{-7}$ )	2459825.45499( $\pm 0.00016$ )	$5.54(\pm 0.33) \times 10^{-10}$	$1.50 \times 10^{-7}$	—	—
LEBS-08	0.3721811( $\pm 6.97 \times 10^{-8}$ )	2459825.50811( $\pm 0.00012$ )	$2.50(\pm 0.08) \times 10^{-10}$	$1.35 \times 10^{-7}$	—	—
LEBS-09	2.2746678( $\pm 2.27 \times 10^{-6}$ )	2459827.54936( $\pm 0.00107$ )	$-3.60(\pm 1.38) \times 10^{-9}$	$-3.65 \times 10^{-8}$	$9.03 \times 10^7$	$5.07 \times 10^6$
LEBS-10	0.2470799( $\pm 1.00 \times 10^{-8}$ )	2459825.34987( $\pm 0.00011$ )	—	—	—	—
LEBS-11	0.4339908( $\pm 1.93 \times 10^{-7}$ )	2459825.66162( $\pm 0.00021$ )	$-7.30(\pm 0.28) \times 10^{-10}$	$-2.03 \times 10^{-9}$	$3.69 \times 10^6$	$1.19 \times 10^6$
LEBS-12	0.5143119( $\pm 3.00 \times 10^{-8}$ )	2459825.48370( $\pm 0.00009$ )	—	—	—	—
LEBS-16	0.3182739( $\pm 3.20 \times 10^{-7}$ )	2459464.26661( $\pm 0.00108$ )	$-3.78(\pm 3.24) \times 10^{-11}$	$-8.63 \times 10^{-7}$	$1.16 \times 10^6$	$4.04 \times 10^6$
LEBS-20	0.3457552( $\pm 9.23 \times 10^{-8}$ )	2459825.47218( $\pm 0.00016$ )	$-2.62(\pm 0.10) \times 10^{-10}$	$-5.53 \times 10^{-7}$	$1.79 \times 10^6$	$1.16 \times 10^7$
LEBS-22	0.4003590( $\pm 2.63 \times 10^{-7}$ )	2459825.48997( $\pm 0.00038$ )	$-5.04(\pm 0.34) \times 10^{-10}$	$-1.27 \times 10^{-7}$	$1.13 \times 10^7$	$3.00 \times 10^7$
LEBS-24	0.3970362( $\pm 4.53 \times 10^{-6}$ )	2459825.66896( $\pm 0.02797$ )	$-1.55(\pm 0.13) \times 10^{-10}$	$-8.50 \times 10^{-8}$	$1.18 \times 10^7$	$3.00 \times 10^7$
LEBS-25	0.4368378( $\pm 1.72 \times 10^{-7}$ )	2459825.76771( $\pm 0.00016$ )	$3.18(\pm 0.26) \times 10^{-10}$	$9.69 \times 10^{-8}$	—	—
LEBS-26(P)	21.0717501( $\pm 1.09 \times 10^{-6}$ )	2459832.63337( $\pm 0.00125$ )	—	—	—	—
LEBS-26(S)	21.0717467( $\pm 1.19 \times 10^{-6}$ )	2459838.35176( $\pm 0.00083$ )	—	—	—	—
LEBS-28	0.4167704( $\pm 2.74 \times 10^{-6}$ )	2459825.63610( $\pm 0.00358$ )	$-6.62(\pm 3.74) \times 10^{-10}$	$-1.93 \times 10^{-7}$	$7.14 \times 10^6$	$5.01 \times 10^7$
LEBS-29	5.1008655( $\pm 7.34 \times 10^{-6}$ )	2459827.46437( $\pm 0.00561$ )	—	—	—	—
LEBS-33	0.5325326( $\pm 7.00 \times 10^{-8}$ )	2459825.76391( $\pm 0.00012$ )	—	—	—	—
LEBS-34	0.3933864( $\pm 1.58 \times 10^{-7}$ )	2459825.37641( $\pm 0.00016$ )	$-3.72(\pm 0.21) \times 10^{-10}$	$-6.19 \times 10^{-8}$	$1.96 \times 10^7$	$1.45 \times 10^7$
LEBS-39	0.3906593( $\pm 2.25 \times 10^{-7}$ )	2459826.39745( $\pm 0.00021$ )	$5.96(\pm 0.30) \times 10^{-10}$	$3.34 \times 10^{-7}$	—	—
LEBS-42	0.2669553( $\pm 4$ )					

" $P_C$  (days)" and " $T_C$  (days)" represent the corrected value of the initial epoch and the orbital period, respectively. " $\beta$  (d/yr)" represents the long-term changing rate of the orbital period. " $dM_1/dt$  ( $M_\odot$ /yr)" represents the rate of material transfer. " $\tau$  (yr)" and " $\tau_{th}$  (yr)" represent the material transfer time-scale and thermal time-scale, respectively. "A", " $P_{mod}$ ", and " $\varphi$ " represent the quasi-sinusoidal change's amplitude, period, and initial phase.

We detected 53 variable stars by analyzing photometric data observed by the 10 cm telescope for 13 days and by the *TESS* sky survey. 48 are EBs, and 2 are newly discovered. Multi-band light curves and radial velocity curves were used to determine the orbital parameters and absolute parameters of 11 targets. For 35 targets without radial velocity curves and 2 targets with unavailable radial velocity curves, we used the q-search method or the temperature ratio method to determine the initial mass ratios and obtained their orbital parameters using the W-D Code. Based on the orbital parameters of 48 EBs, 15 EBs belonged to detached systems, 1 to semi-detached systems, and 32 to contact systems. LEBS-06 is a detached system with spots on both components and exhibits double-peaked H $\alpha$  emission lines. In binary systems, double-peaked H $\alpha$  emission lines are typically the result of either an accretion disk or chromospheric activity. If the double-peaked H $\alpha$  emission lines are caused by the accretion disk, they would generally display a broader velocity range and a more symmetrical profile (Marsango et al. 2024), with the position of the emission lines remaining constant across all observed phases (Zhang et al. 2024). However, the double-peaked H $\alpha$  emission lines of LEBS-06 only appear around phases 0.25 and 0.75, with an asymmetric profile, and their position is variable. Therefore, we believe that the double-peaked H $\alpha$  emission lines of LEBS-06 are due to the intense chromospheric activity of the two components. LEBS-21, LEBS-22, LEBS-28, LEBS-34, LEBS-41, and LEBS-48 are totally eclipsing contact systems, indicating their orbital parameters determined only by photometric data are reliable (Terrell & Wilson 2005; Li et al. 2021a). A combined analysis of photometric and spectroscopic observations by Gürol et al. (2011) indicated that LEBS-04 was an overcontact system, with a mass ratio of  $0.243(\pm 0.008)$ , a contact degree of 32.1%, and a orbital inclination of  $62.214(\pm 0.368)^\circ$ . Our study shows that its mass ratio is  $0.214(\pm 0.002)$ , its orbital inclination is  $61.645(\pm 0.088)^\circ$ , and its contact degree is  $41.0(\pm 4.4)\%$ . Kjurkchieva et al. (2019) calculated the orbit parameters of LEBS-20 ( $q=1.256(\pm 0.004)$ ,  $i=80.37(\pm 0.5)^\circ$ ,  $f=2.6\%$ ). Our work obtained the similar results ( $q=1.474(\pm 0.012)$ ,  $i=80.463(\pm 0.073)^\circ$ ,  $f=2.7(\pm 3.1)\%$ ). Moreover, the light curves in our work showed a weak O’Connell effect, so we added a spot on its primary star. Given the impact of different precision in observational data and the impact of the starspots, our research results are basically consistent with those determined by previous studies. LEBS-31 had a W UMa-type light curve, but the W-D result suggested that it was a detached system. A high fill-out factor (98.0, 98.5%) for the primary and secondary components indicated that it may evolve into a contact system in the near future. LEBS-18 had a similar fill-out factor (77.3, 99.3%) of their primary and secondary components. LEBS-40 showed a  $\beta$  Lyrae light curve, but the W-D result indicated that it is a contact binary with a contact degree of 7.2%, implying that it is a newly formed contact system.

### 6.1. Absolute physical parameters

Absolute physical parameters help to study the formation, structure, evolution, and ultimate fate of EBs (Shokry et al. 2018; Li et al. 2021a). The absolute physical parameters of the 11 targets with radial velocity curves can be obtained directly by W-D results. For 35 targets without radial velocity curves and 2 targets with unavailable radial velocity curves, assuming that the more massive components of each target are main-sequence stars and primary components, based on the temperature-to-mass relationship (Pecaut & Mamajek 2013) and the mass ratios, the masses of the two components were calculated. According to Kepler’s third law ( $M_1 + M_2 = \frac{0.0134a^3}{p^2}$ ), we obtained the semi-major axis  $a$ . The radius  $R_{1,2}$  was given by  $R_{1,2} = a \times r_{1,2}$ . Then, we used  $L_{1,2} = (R_{1,2}/R_\odot)^2(T_{1,2}/T_\odot)^4$  to obtain the luminosity  $L_{1,2}$ . The errors of the above parameters were calculated with the error transfer formula. The absolute parameters of all targets are shown in Table 6.

### 6.2. Orbital period variations

#### 6.2.1. Long-term increase or decrease

There are many reasons for orbital period variations. Typically, the long-term increase in the period can be explained by material transfer from the less massive component to the more massive one. At the same time, the long-term decrease in orbital period can be explained by material transfer from the more massive component to the less one, angular momentum loss, or both. If the period variation is caused by material transfer, assuming that the angular momentum and total mass are constant, the rate of material transfer can be calculated by the equation (Kwee 1958)

$$\frac{\dot{P}}{P} = -3\dot{M}_1 \left( \frac{1}{M_1} - \frac{1}{M_2} \right). \quad (8)$$

To further determine the reason for the long-term decrease in orbital period, the material transfer time-scale  $\tau$  and the thermal time-scale  $\tau_{th}$  were calculated by the equation

$$\tau \sim \frac{M_1}{\dot{M}_1}, \tau_{th} = \frac{GM_1^2}{R_1 L_1}. \quad (9)$$

The rate of material transfer  $\dot{M}_1$ , the mass transfer time-scale  $\tau$ , and the thermal time-scale  $\tau_{th}$  are shown in Table 5. As can be seen, for LEBS-04, LEBS-11, LEBS-16, LEBS-22, LEBS-24, LEBS-34, and LEBS-42, the time-scale  $\tau$  and the thermal time-scale  $\tau_{th}$  are within the same order of magnitude, implying that the long-term decrease in orbital period is caused by material transfer. For LEBS-09, LEBS-20, LEBS-28, and LEBS-47, the time-scale  $\tau$  and the thermal time-scale  $\tau_{th}$  are not within the same order of magnitude, implying that the long-term decrease in orbital period is attributed to the loss of orbital angular momentum or a combination of both.

### 6.2.2. Possible mechanisms of the cyclic oscillation

The O - C curves of LEBS-14 and LEBS-41 showed a quasi-periodic variation. For LEBS-14,  $P_{mod} = 20.72(\pm 1.12)$  yr and an amplitude of  $A = 0.07(\pm 0.01)$  days. For LEBS-41,  $P_{mod} = 32.52(\pm 21.68)$  yr and an amplitude of  $A = 0.02(\pm 0.03)$  days. Because the amplitude of the periodic oscillation for LEBS-41 is consistent with zero, the reason for its periodic oscillation is not discussed. Currently, cyclic oscillation can be caused by the magnetic activity of one or both components (Applegate 1992) or the light travel time effect (LTTE) via a third body (Yang et al. 2012; Li et al. 2021b).

If the cyclic modulation is caused by magnetic activity, the variation in the magnetic quadrupole moment ( $\Delta Q$ ) can be calculated according to the following equation by Applegate (1992)

$$\frac{\Delta P}{P} = \frac{2\pi \times A}{P_{mod}} = -9\left(\frac{R}{a}\right)^2 \frac{\Delta Q}{MR^2}, \quad (10)$$

where  $M$ ,  $R$ , and  $a$  are mass, radii of the active component, and the semi-major axis of the targets. For LEBS-14, the values of  $\Delta Q$  were calculated as,  $\Delta Q_1 = 3.350(\pm 0.126) \times 10^{50} g cm^2$  and  $\Delta Q_2 = 6.472(\pm 0.244) \times 10^{49} g cm^2$ . These results are clearly smaller than the typical values of  $10^{51} \sim 10^{52} g cm^2$  for close binaries (Lanza & Rodonò 1999). Therefore, the Applegate mechanism is not reasonable to be used to explain the periodic variations.

Another possible mechanism is the LTTE. The distance of the binary system to the barycenter of the triple system was calculated with the equation

$$a_{12} \sin i_3 = A \times c, \quad (11)$$

where  $A$  is the amplitude of the O - C oscillation and  $c$  is the speed of the light. We derived  $a_{12} \sin i_3 = 11.919(\pm 1.093)$  AU. The mass function of the third body  $f(M_3)$  was calculated by the follow equation

$$f(M_3) = \frac{(M_3 \sin i_3)^3}{(M_1 + M_2 + M_3)^2} = \frac{4\pi^2}{GP_3^2} \times (a_{12} \sin i_3)^3, \quad (12)$$

the mass function of the third body was determined as  $f(M_3) = 3.943(\pm 1.085) M_\odot$ . When the orbital inclination of the third body ( $i_3$ ) was  $90^\circ$ , the minimum mass of the third body was determined to be  $M_{3min} = 5.570(\pm 1.953) M_\odot$ , which suggests that it is likely a black hole. This makes LEBS-14 a valuable subject for study, necessitating long-term observational follow-up to confirm the current conclusions of the O-C analysis.

### 6.3. Evolutionary state

To study the evolutionary state of the EBs, we plotted their mass-luminosities (M-L) and mass-radius (M-R) distributions as in Figure 6, in which evolutionary tracks for solar chemical compositions (as colored dotted lines) are taken from Girardi et al. (2000), the zero-age main sequence (ZAMS) (as solid lines) and the terminal-age main sequence (TAMS) (as dashed lines) are plotted. The triangular and circular symbols denote targets with and without radial velocity curves, respectively. The solid and hollow symbols denote the more and less massive components, respectively. The red, blue, and green symbols denote detached, contact, and semi-detached systems, respectively. As shown in the figure, the more massive primary stars are closer to ZAMS than the less massive secondary stars, and the less massive secondary stars are closer to the TAMS, which means that the more massive primary stars are less evolved than secondaries. In binary systems, the initially more massive component evolves more rapidly, expanding to fill its Roche Lobe and transferring material to the less massive component. This process results in the less massive component gaining mass, while the more massive component concurrently loses mass, leading to a reversal in their mass ratio (Coughlin et al. 2008). Therefore, in semi-detached and contact systems, due to material transfer and the reversal of the mass ratio, the initial less massive component becomes the more massive one and is now at the main sequence stage. Conversely, the initial more massive component has essentially evolved off the main sequence stage. For detached systems with rapidly evolving secondary stars, we think it may be because they are currently in the stage of contact broken stage during Thermal Relaxation Oscillations (TRO) (Lucy 1976; Flannery 1976; Robertson & Eggleton 1977), which is also caused by a previous reversal in the

**Table 6.** Absolute parameters of 48 EBs.

Target	$M_1(M_\odot)$	$M_2(M_\odot)$	$a(R_\odot)$	$R_1(R_\odot)$	$R_2(R_\odot)$	$L_1(L_\odot)$	$L_2(L_\odot)$
LEBS-01	1.303(±0.108)	0.267(±0.025)	3.524(±0.103)	1.931(±0.058)	0.980(±0.039)	7.910(±0.611)	1.259(±0.146)
LEBS-02	2.600(±0.131)	1.658(±0.108)	7.407(±0.139)	3.176(±0.082)	2.593(±0.104)	20.080(±1.547)	11.483(±1.773)
LEBS-03	1.298(±0.189)	0.587(±0.080)	9.306(±0.444)	1.604(±0.087)	1.408(±0.070)	2.418(±0.360)	2.033(±0.247)
LEBS-04	0.993(±0.089)	0.212(±0.021)	2.509(±0.077)	1.346(±0.044)	0.695(±0.038)	2.773(±0.325)	0.680(±0.144)
LEBS-05	1.062(±0.040)	0.201(±0.008)	3.264(±0.042)	1.753(±0.024)	0.841(±0.019)	6.198(±0.226)	0.935(±0.062)
LEBS-06	0.710(±0.011)	0.653(±0.015)	8.329(±0.053)	0.838(±0.007)	0.745(±0.007)	0.424(±0.051)	0.277(±0.056)
LEBS-07	1.353(±0.064)	0.505(±0.028)	3.685(±0.061)	1.854(±0.035)	1.235(±0.042)	6.179(±0.335)	2.850(±0.300)
LEBS-08	0.932(±0.010)	0.370(±0.001)	2.377(±0.007)	1.114(±0.011)	0.733(±0.004)	1.038(±0.152)	0.575(±0.049)
LEBS-09	3.295(±0.125)	0.381(±0.018)	11.234(±0.146)	4.139(±0.065)	2.403(±0.153)	70.647(±5.172)	4.931(±1.008)
LEBS-10	0.780(±0.082)	0.350(±0.036)	1.726(±0.060)	0.793(±0.030)	0.552(±0.020)	0.217(±0.039)	0.128(±0.017)
LEBS-11	1.330(±0.019)	0.848(±0.085)	5.927(±0.002)	2.582(±0.005)	1.882(±0.003)	13.54(±0.250)	2.031(±0.075)
LEBS-12	1.610(±0.110)	0.110(±0.001)	3.238(±0.001)	2.040(±0.003)	0.664(±0.048)	9.831(±0.327)	0.988(±0.235)
LEBS-13	0.940(±0.040)	0.240(±0.004)	2.159(±0.002)	1.127(±0.018)	0.637(±0.004)	1.014(±0.078)	0.401(±0.013)
LEBS-14	1.030(±0.030)	0.200(±0.001)	2.632(±0.001)	1.395(±0.007)	0.655(±0.002)	2.059(±0.386)	0.973(±0.099)
LEBS-15	1.380(±0.050)	0.760(±0.012)	2.854(±0.005)	1.262(±0.007)	0.953(±0.024)	2.817(±0.164)	1.418(±0.218)
LEBS-16	1.000(±0.010)	0.950(±0.106)	2.452(±0.044)	1.018(±0.152)	0.954(±0.042)	1.019(±0.404)	1.065(±0.137)
LEBS-17	1.080(±0.020)	1.060(±0.004)	35.800(±0.024)	1.038(±0.360)	0.752(±0.360)	1.221(±0.886)	0.399(±0.490)
LEBS-18	1.750(±0.140)	0.260(±0.204)	5.614(±0.190)	2.234(±0.108)	1.325(±0.056)	12.951(±1.637)	2.148(±0.465)
LEBS-19	1.330(±0.080)	1.180(±0.047)	14.700(±0.092)	1.705(±0.018)	0.941(±0.013)	4.637(±0.313)	1.169(±0.146)
LEBS-20	0.990(±0.010)	0.670(±0.005)	2.456(±0.003)	1.017(±0.010)	0.850(±0.003)	1.007(±0.081)	0.728(±0.030)
LEBS-21	0.880(±0.020)	0.250(±0.005)	2.195(±0.003)	1.089(±0.007)	0.613(±0.023)	0.843(±0.169)	0.332(±0.052)
LEBS-22	1.440(±0.020)	0.270(±0.011)	2.735(±0.006)	1.499(±0.010)	0.722(±0.071)	4.226(±0.526)	0.993(±0.246)
LEBS-23	0.700(±0.010)	0.360(±0.003)	1.782(±0.002)	0.784(±0.006)	0.577(±0.003)	0.202(±0.043)	0.149(±0.016)
LEBS-24	1.000(±0.030)	0.330(±0.008)	2.216(±0.005)	1.079(±0.004)	0.663(±0.004)	1.195(±0.058)	0.575(±0.015)
LEBS-25	1.460(±0.040)	0.360(±0.008)	2.959(±0.005)	1.489(±0.008)	0.784(±0.035)	4.401(±0.261)	1.163(±0.230)
LEBS-26	0.980(±0.005)	0.850(±0.001)	39.287(±0.007)	0.864(±0.045)	0.825(±0.045)	0.693(±0.108)	0.595(±0.163)
LEBS-27	1.060(±0.020)	0.190(±0.024)	2.174(±0.014)	1.157(±0.031)	0.587(±0.179)	1.486(±0.092)	0.382(±0.278)
LEBS-28	1.380(±0.060)	0.320(±0.002)	2.804(±0.001)	1.477(±0.003)	0.788(±0.011)	3.921(±0.147)	1.021(±0.098)
LEBS-29	1.440(±0.020)	1.400(±0.002)	17.668(±0.004)	1.343(±0.007)	1.908(±0.006)	3.370(±0.239)	6.521(±0.739)
LEBS-30	1.880(±0.050)	1.450(±0.002)	8.696(±0.002)	2.113(±0.032)	1.800(±0.027)	17.8127(±1.946)	2.309(±0.524)
LEBS-31	0.970(±0.020)	0.180(±0.001)	1.777(±0.001)	0.945(±0.002)	0.434(±0.002)	0.785(±0.014)	0.145(±0.014)
LEBS-32	0.820(±0.040)	0.710(±0.042)	4.871(±0.045)	0.779(±0.021)	0.794(±0.039)	0.369(±0.087)	0.339(±0.144)
LEBS-33	1.500(±0.110)	0.290(±0.062)	3.359(±0.039)	1.565(±0.028)	0.893(±0.018)	5.368(±0.379)	0.230(±0.034)
LEBS-34	1.210(±0.040)	0.180(±0.001)	2.523(±0.001)	1.458(±0.009)	0.691(±0.027)	2.995(±0.111)	0.695(±0.108)
LEBS-35	0.620(±0.030)	0.610(±0.001)	2.541(±0.000)	0.363(±0.001)	0.231(±0.002)	0.029(±0.003)	0.015(±0.001)
LEBS-36	1.980(±0.070)	0.660(±0.090)	8.819(±0.100)	1.676(±0.085)	2.372(±0.587)	16.219(±2.441)	4.788(±3.083)
LEBS-37	1.460(±0.020)	0.230(±0.015)	11.614(±0.033)	1.521(±0.016)	0.743(±0.027)	4.449(±0.381)	0.804(±0.176)
LEBS-38	0.880(±0.020)	0.440(±0.038)	2.024(±0.019)	0.921(±0.091)	0.721(±0.028)	0.579(±0.185)	0.370(±0.039)
LEBS-39	1.180(±0.050)	0.440(±0.003)	2.642(±0.002)	1.245(±0.009)	0.790(±0.003)	1.965(±0.408)	0.894(±0.091)
LEBS-40	0.900(±0.020)	0.270(±0.002)	2.314(±0.001)	1.136(±0.007)	0.653(±0.002)	0.958(±0.131)	1.012(±0.066)
LEBS-41	1.030(±0.030)	0.250(±0.003)	2.469(±0.002)	1.289(±0.006)	0.701(±0.023)	1.775(±0.105)	0.477(±0.081)
LEBS-42	0.780(±0.040)	0.340(±0.003)	1.813(±0.001)	0.834(±0.007)	0.566(±0.001)	0.349(±0.085)	0.238(±0.033)
LEBS-43	0.780(±0.040)	0.500(±0.011)	1.812(±0.005)	0.790(±0.021)	0.641(±0.006)	0.320(±0.112)	0.231(±0.041)
LEBS-44	0.700(±0.030)	0.590(±0.044)	4.190(±0.047)	0.629(±0.037)	0.884(±0.022)	0.147(±0.023)	0.428(±0.024)
LEBS-45	0.780(±0.040)	0.280(±0.016)	1.922(±0.010)	0.924(±0.057)	0.603(±0.017)	0.456(±0.070)	0.273(±0.016)
LEBS-46	1.250(±0.080)	0.580(±0.024)	2.747(±0.012)	1.327(±0.017)	0.970(±0.066)	2.660(±0.299)	1.410(±0.439)
LEBS-47	1.440(±0.020)	0.700(±0.011)	4.997(±0.009)	2.234(±0.011)	1.599(±0.040)	9.472(±0.320)	3.395(±0.368)
LEBS-48	0.880(±0.020)	0.210(±0.003)	2.004(±0.002)	1.026(±0.014)	0.531(±0.003)	0.752(±0.100)	0.246(±0.017)

Assuming that the more massive components are the primary components. " $M_1(M_\odot)$ ", " $R_1(R_\odot)$ ", and " $L_1(L_\odot)$ " represent the mass, radius, and luminosity of the primary component. " $M_2(M_\odot)$ ", " $R_2(R_\odot)$ ", and " $L_2(L_\odot)$ " represent the mass, radius, and luminosity of the secondary component. "a" represents the semi-major axis.

mass ratio. As shown in Figure 6, the less massive components are located outside the evolutionary models, not because they have evolved to this position, but because the material transfer between the two components, which results in the less massive components exhibiting over-luminosity and over-size relative to main sequence stars of the same mass.

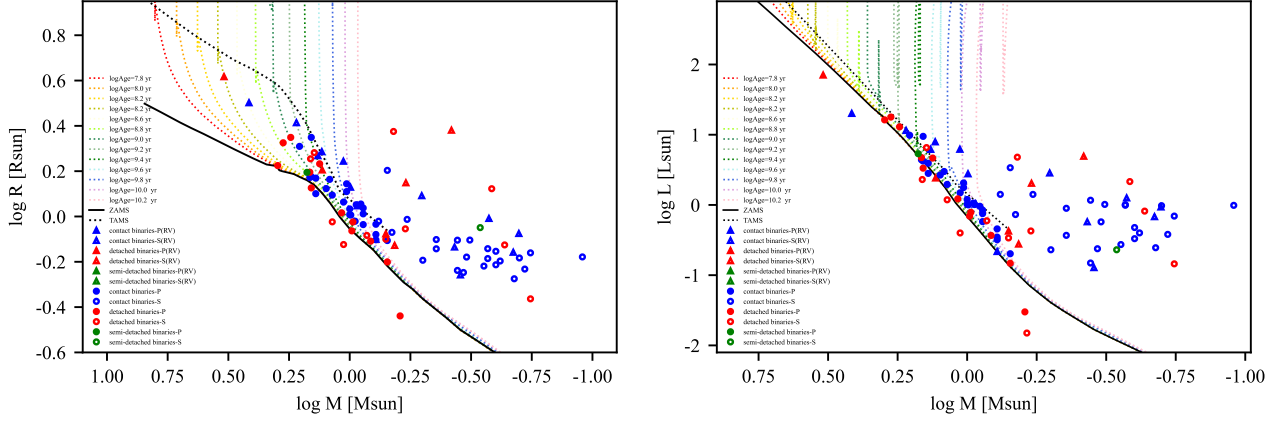


**Figure 6.** The M-R and M-L distributions for EBs. The colored dotted lines indicate the evolutionary tracks for solar chemical compositions. The solid and dashed lines indicate the zero-age main sequence (ZAMS) and the terminal-age main sequence (TAMS), respectively. The triangular and circular symbols denote targets with and without radial velocity curves, respectively. The solid and hollow symbols denote the more and less massive components, respectively. The red, blue, and green symbols denote detached, contact, and semi-detached systems, respectively.

Then, we calculated the orbital angular momentum  $J_{orb}$  using the following equation (Eker et al. 2006):

$$J_{orb} = \frac{q}{(1+q)^2} \sqrt[3]{\frac{G^2}{2\pi} M_T^5 P} \quad (13)$$

where  $M_T$  is the total mass of the binary,  $P$  is the orbital period, and  $q$  is the mass ratio. The total mass versus orbital angular momentum distribution is plotted in Figure 7. The dashed line indicates the boundary line between the detached and contact binaries (Eker et al. 2006). The solid and hollow symbols indicate targets with and without radial velocity curves, respectively. The red, blue, and green symbols denote detached, contact, and semi-detached systems, respectively. Almost all contact binaries are below the boundary line, representing a smaller orbital angular momentum for the contact binary with the same total mass. The reason for this phenomenon is the angular momentum loss due to mass loss or magnetic stellar wind during the formation of contact binaries. This conclusion is consistent with previous studies (e.g., Li et al. 2021a).

In conclusion, 48 EBs were detected around the field, RA:  $23^h01^m51.00^s$ , Dec:  $+34^\circ36'45''$ . The orbital parameters were determined, with 15 EBs belonging to detached systems, 1 to semi-detached systems, and 32 to contact systems. The orbital period variation was analyzed using the O-C method. Additionally, chromospheric activity in the LAMOST medium-resolution spectra was analyzed. Finally, the evolutionary states were discussed.

## 7. DATA AVAILABILITY

The 10 cm telescope data and *TESS* data used in this research can be downloaded through China VO (<https://nadc.china-vo.org/res/r101438/>).

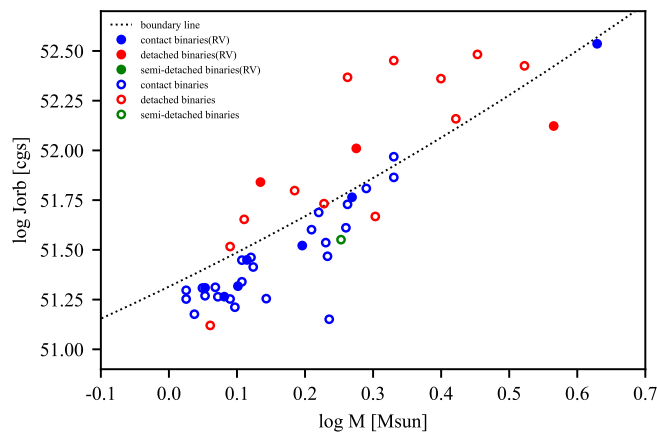


**Figure 7.** The relation between orbital angular momentum and total mass for EBs. The dashed line indicates the boundary line between the detached and contact binaries. The solid and hollow symbols indicate targets with and without radial velocity curves, respectively. The red, blue, and green symbols denote detached, contact, and semi-detached systems, respectively.

We are grateful to the reviewer for the valuable suggestions and comments, which has significantly contributed to the enhancement of this manuscript. This work was supported by National Natural Science Foundation of China (NSFC) (No. 12273018), and the Joint Research Fund in Astronomy (No.U1931103) under cooperative agreement between NSFC and Chinese Academy of Sciences (CAS), and by the Qilu Young Researcher Project of Shandong University, and by Young Data Scientist Project of the National Astronomical Data Center and by the Cultivation Project for LAMOST Scientific Payoff and Research Achievement of CAMSCAS, and by the Chinese Academy of Science Interdisciplinary Innovation Team. The calculations in this work were carried out at Supercomputing Center of Shandong University, Weihai.

The spectral data were provided by Guoshoujing Telescope (the Large Sky Area Multi-Object Fiber Spectroscopic Telescope LAMOST), which is a national major scientific project built by the Chinese Academy of Sciences. Funding for the project has been provided by the National Development and Reform Commission. LAMOST is operated and managed by the National Astronomical Observatories, Chinese Academy of Sciences.

This work includes data collected by the TESS mission. Funding for the TESS mission is provided by NASA Science Mission Directorate. We acknowledge the TESS team for its support of this work. We thank Las Cumbres Observatory and its staff for their continued support of ASAS-SN. ASAS-SN is funded in part by the Gordon and Betty Moore Foundation through grant nos. GBMF5490 and GBMF10501 to the Ohio State University, and also funded in part by the Alfred P. Sloan Foundation grant no.G-2021-14192. This paper makes use of data from ZTF. ZTF is supported by the National Science Foundation under grant no.AST-1440341 and a collaboration including Caltech, IPAC, the Weizmann Institute for Science, the Oskar Klein Center at Stockholm University, the University of Maryland, the University of Washington, Deutsches Elektronen-Synchrotron and Humboldt University, Los Alamos National Laboratories, the TANGO Consortium of Taiwan, the University of Wisconsin at Milwaukee, and Lawrence Berkeley National Laboratories. Operations are conducted by COO, IPAC, and UW. This publication makes use of data products from the AAVSO Photometric All Sky Survey (APASS). Funded by the Robert Martin Ayers Sciences Fund and the National Science Foundation. This publication makes use of data products from the Two Micron All Sky Survey, which is a joint project of the University of Massachusetts and the Infrared Processing and Analysis Center/California Institute of Technology, funded by the National Aeronautics and Space Administration and the Science Foundation. This paper makes use of data from the DR1 of the WASP data, Butters et al. (2010) as provided by the WASP consortium, and the computing and storage facilities at the CERIT Scientific Cloud, reg. no. CZ.1.05/3.2.00/08.0144, which is operated by Masaryk University, Czech Republic. This work has made use of data from the European Space Agency (ESA) mission Gaia (<https://www.cosmos.esa.int/gaia>), processed by the Gaia Data Processing and Analysis Consortium (DPAC,<https://www.cosmos.esa.int/web/gaia/dpac/consortium>). Funding for the DPAC has been provided by national institutions, in particular the institutions participating in the Gaia Multilateral Agreement.

## REFERENCES



- Arbutina, B. 2007, *MNRAS*, 377, 1635.  
doi:10.1111/j.1365-2966.2007.11723.x
- Arbutina, B. 2009, *MNRAS*, 394, 501.  
doi:10.1111/j.1365-2966.2008.14332.x
- Barden, S. C. 1985, *ApJ*, 295, 162. doi:10.1086/163361
- Bellm, E. C., Kulkarni, S. R., Graham, M. J., et al. 2019, *PASP*, 131, 018002. doi:10.1088/1538-3873/aaecbe
- Binnendijk, L. 1964, *AJ*, 69, 154. doi:10.1086/109252
- Bonanos, A. Z., Stanek, K. Z., Kudritzki, R. P., et al. 2006, *ApJ*, 652, 313. doi:10.1086/508140
- Bradstreet, D. H. & Guinan, E. F. 1994, *Interacting Binary Stars*, 56, 228
- Brasseur, C. E., Phillip, C., Fleming, S. W., et al. 2019, *Astrophysics Source Code Library*. ascl:1905.007
- Butters, O. W., West, R. G., Anderson, D. R., et al. 2010, *A&A*, 520, L10. doi:10.1051/0004-6361/201015655
- Caton, D., Gentry, D. R., Samec, R. G., et al. 2019, *PASP*, 131, 054203. doi:10.1088/1538-3873/aafb8f
- Caton, D., Gentry, D. R., Samec, R. G., et al. 2019, *PASP*, 131, 054203. doi:10.1088/1538-3873/aafb8f
- Christopoulou, P.-E. & Papageorgiou, A. 2013, *AJ*, 146, 157. doi:10.1088/0004-6256/146/6/157
- Coughlin, J. L., Dale, H. A., & Williamon, R. M. 2008, *AJ*, 136, 1089. doi:10.1088/0004-6256/136/3/1089
- Cutri, R. M., Skrutskie, M. F., van Dyk, S., et al. 2003, "The IRSA 2MASS All-Sky Point Source Catalog, NASA/IPAC Infrared Science Archive. jA
- Cui, X.-Q., Zhao, Y.-H., Chu, Y.-Q., et al. 2012, *Research in Astronomy and Astrophysics*, 12, 1197. doi:10.1088/1674-4527/12/9/003
- Eker, Z., Demircan, O., Bilir, S., et al. 2006, *MNRAS*, 373, 1483. doi:10.1111/j.1365-2966.2006.11073.x
- Fang, X.-S., Zhao, G., Zhao, J.-K., et al. 2018, *MNRAS*, 476, 908. doi:10.1093/mnras/sty212
- Feng, G., Esamdin, A., Fu, J., et al. 2021, *MNRAS*, 508, 529. doi:10.1093/mnras/stab2063
- Flannery, B. P. 1976, *ApJ*, 205, 217. doi:10.1086/154266
- Gaia Collaboration 2022, *VizieR Online Data Catalog*, 1358. I/358
- Gao, X., Li, K., Gao, X., et al. 2021, *Research in Astronomy and Astrophysics*, 21, 193. doi:10.1088/1674-4527/21/8/193
- Girardi, L., Bressan, A., Bertelli, G., et al. 2000, *A&AS*, 141, 371. doi:10.1051/aas:2000126
- Green, G. M., Schlafly, E., Zucker, C., et al. 2019, *ApJ*, 887, 93. doi:10.3847/1538-4357/ab5362
- Guinan, E. F., Fitzpatrick, E. L., DeWarf, L. E., et al. 1998, *ApJL*, 509, L21. doi:10.1086/311760
- Guo, D.-F., Li, K., Gao, X., et al. 2020, *MNRAS*, 497, 3381. doi:10.1093/mnras/staa2170
- Guo, D.-F., Li, K., Liu, F., et al. 2022, *MNRAS*, 517, 1928. doi:10.1093/mnras/stac2811
- Gürol, B., Terzioğlu, Z., Gürsoytrak, S. H., et al. 2011, *Astronomische Nachrichten*, 332, 690. doi:10.1002/asna.201111563
- Hall, J. C. 2008, *Living Reviews in Solar Physics*, 5, 2. doi:10.12942/lrsp-2008-2
- Henden, A. A., Levine, S., Terrell, D., et al. 2015, *AAS Meeting Abstracts*
- Henden, A. A., Templeton, M., Terrell, D., et al. 2016, *VizieR Online Data Catalog*, II/336
- Hubscher, J. 2016, *Information Bulletin on Variable Stars*, 6157, 1
- Husser, T.-O., Wende-von Berg, S., Dreizler, S., et al. 2013, *A&A*, 553, A6. doi:10.1051/0004-6361/201219058
- Iglesias-Marzoa, R., López-Morales, M., & Jesús Arévalo Morales, M. 2015, *PASP*, 127, 567. doi:10.1086/682056
- Jatmiko, A. T. P., Yusuf, M., & Putra, M. 2019, *Journal of Physics Conference Series*, 1245, 012019. doi:10.1088/1742-6596/1245/1/012019
- Jayasinghe, T., Kochanek, C. S., Stanek, K. Z., et al. 2018, *MNRAS*, 477, 3145. doi:10.1093/mnras/sty838
- Jiang, D., Han, Z., Wang, J., et al. 2010, *MNRAS*, 405, 2485. doi:10.1111/j.1365-2966.2010.16615.x
- Kjurkchieva, D. & Vasileva, D. 2015, *PASA*, 32, e023. doi:10.1017/pasa.2015.23
- Kjurkchieva, D. P. & Vasileva, D. L. 2018, *Ap&SS*, 363, 19. doi:10.1007/s10509-017-3239-0
- Kjurkchieva, D. P., Popov, V. A., Eneva, Y., et al. 2019, *Research in Astronomy and Astrophysics*, 19, 014. doi:10.1088/1674-4527/19/1/14
- Knote, M. F., Caballero-Nieves, S. M., Gokhale, V., et al. 2022, *ApJS*, 262, 10. doi:10.3847/1538-4365/ac770f
- Kochanek, C. S., Shappee, B. J., Stanek, K. Z., et al. 2017, *PASP*, 129, 104502. doi:10.1088/1538-3873/aa80d9
- Kopal, Z. 1955, *Annales d'Astrophysique*, 18, 379
- Kwee, K. K. & van Woerden, H. 1956, *BAN*, 12, 327
- Kwee, K. K. 1958, *BAN*, 14, 131
- Lanza, A. F. & Rodonò, M. 1999, *A&A*, 349, 887
- Li, C.-Q., Shi, J.-R., Yan, H.-L., et al. 2021, *ApJS*, 256, 31. doi:10.3847/1538-4365/ac22a8
- Li, L. & Zhang, F. 2006, *MNRAS*, 369, 2001. doi:10.1111/j.1365-2966.2006.10462.x
- Li, K. & Qian, S.-B. 2013, *NewA*, 21, 46. doi:10.1016/j.newast.2012.11.003
- Li, K., Qian, S.-B., Hu, S.-M., et al. 2014, *AJ*, 147, 98. doi:10.1088/0004-6256/147/5/98
- Li, K., Hu, S., Guo, D., et al. 2015, *NewA*, 41, 17. doi:10.1016/j.newast.2015.04.010
- Li, K., Gao, D.-Y., Hu, S.-M., et al. 2016, *Ap&SS*, 361, 63. doi:10.1007/s10509-016-2649-8
- Li, K., Kim, C.-H., Xia, Q.-Q., et al. 2020, *AJ*, 159, 189. doi:10.3847/1538-3881/ab7cda

- Li, K., Xia, Q.-Q., Kim, C.-H., et al. 2021a, *AJ*, 162, 13.  
doi:10.3847/1538-3881/abfc53
- Li, K., Xia, Q.-Q., Kim, C.-H., et al. 2021b, *ApJ*, 922, 122.  
doi:10.3847/1538-4357/ac242f
- Li, K., Gao, X., Liu, X.-Y., et al. 2022, *AJ*, 164, 202.  
doi:10.3847/1538-3881/ac8ff2
- Lightkurve Collaboration, Cardoso, J. V. de M., Hedges, C., et al. 2018, *Astrophysics Source Code Library*. ascl:1812.013
- Liu, Q.-Y. & Yang, Y.-L. 2003, *ChJ&A*, 3, 142.  
doi:10.1088/1009-9271/3/2/142
- Liu, X.-Y., Li, K., Michel, R., et al. 2023, *MNRAS*, 519, 5760.  
doi:10.1093/mnras/stad026
- Liu, H.-B., Gu, W.-M., Zhang, Z.-X., et al. 2024, *ApJ*, 969, 114.  
doi:10.3847/1538-4357/ad4c6f
- Long, L., Zhang, L.-yun., Bi, S.-L., et al. 2021, *ApJS*, 253, 51.  
doi:10.3847/1538-4365/abe30b
- Lucy, L. B. 1967, *ZA*, 65, 89
- Lucy, L. B. 1976, *ApJ*, 205, 208. doi:10.1086/154265
- Luo, A.-L., Zhao, Y.-H., Zhao, G., et al. 2015, *Research in Astronomy and Astrophysics*, 15, 1095.  
doi:10.1088/1674-4527/15/8/002
- López-Santiago, J., Montes, D., Gálvez-Ortiz, M. C., et al. 2010, *A&A*, 514, A97. doi:10.1051/0004-6361/200913437
- Maciejewski, G. & Ligeza, P. 2004, *Information Bulletin on Variable Stars*, 5504, 1
- Marsango, D., Schimoia, J. S., Rembold, S. B., et al. 2024, *MNRAS*, 529, 3089. doi:10.1093/mnras/stae694
- Masci, F. J., Laher, R. R., Rusholme, B., et al. 2019, *PASP*, 131, 018003. doi:10.1088/1538-3873/aae8ac
- Matijević, G., Zwitter, T., Munari, U., et al. 2010, *AJ*, 140, 184.  
doi:10.1088/0004-6256/140/1/184
- Mattei, J. A. & Saladyga, M. 1999, *Anni Mirabiles*, 59
- Michel, R., Xia, Q.-Q., & Higuera, J. 2019, *Research in Astronomy and Astrophysics*, 19, 099. doi:10.1088/1674-4527/19/7/99
- Mitnyan, T., Szalai, T., Bódi, A., et al. 2020, *A&A*, 635, A89.  
doi:10.1051/0004-6361/201937214
- Montes, D., Fernández-Figueroa, M. J., De Castro, E., et al. 2000, *A&AS*, 146, 103. doi:10.1051/aas:2000359
- Niarchos, P. G., Hoffmann, M., & Duerbeck, H. W. 1997, *A&AS*, 124, 291. doi:10.1051/aas:1997193
- O'Connell, D. J. K. 1951, *MNRAS*, 111, 642.  
doi:10.1093/mnras/111.6.642
- Oelkers, R. J. & Stassun, K. G. 2018, *AJ*, 156, 132.  
doi:10.3847/1538-3881/aad68e
- Oliphant, T. E. 2007, *Computing in Science and Engineering*, 9, 10. doi:10.1109/MCSE.2007.58
- Özdemir, S., Mayer, P., Drechsel, H., et al. 2003, *A&A*, 403, 675.  
doi:10.1051/0004-6361:20030392
- Paczynski, B. & Sasselov, D. 1997, *Variables Stars and the Astrophysical Returns of the Microlensing Surveys*, 309.  
doi:10.48550/arXiv.astro-ph/9608094
- Panchal, A., Joshi, Y. C., De Cat, P., et al. 2022, *ApJ*, 927, 12.  
doi:10.3847/1538-4357/ac45fb
- Pavlenko, Y. V., Evans, A., Banerjee, D. P. K., et al. 2018, *A&A*, 615, A120. doi:10.1051/0004-6361/201832717
- Pecaut, M. J. & Mamajek, E. E. 2013, *ApJS*, 208, 9.  
doi:10.1088/0067-0049/208/1/9
- Pi, Q.-feng., Zhang, L.-yun., Bi, S.-lan., et al. 2019, *ApJ*, 877, 75. doi:10.3847/1538-4357/ab19c3
- Prša, A. & Zwitter, T. 2005, *ApJ*, 628, 426. doi:10.1086/430591
- Qian, S.-B., Xiang, F.-Y., Zhu, L.-Y., et al. 2007, *AJ*, 133, 357.  
doi:10.1086/509499
- Qian, S.-B., Zhang, J., Wang, J.-J., et al. 2013, *ApJS*, 207, 22.  
doi:10.1088/0067-0049/207/2/22
- Qian, S.-B., He, J.-J., Zhang, J., et al. 2017, *Research in Astronomy and Astrophysics*, 17, 087. doi:10.1088/1674-4527/17/8/87
- Qian, S.-B., Zhu, L.-Y., Liu, L., et al. 2020, *Research in Astronomy and Astrophysics*, 20, 163. doi:10.1088/1674-4527/20/10/163
- Rasio, F. A. 1995, *ApJL*, 444, L41. doi:10.1086/187855
- Ricker, G. R., Winn, J. N., Vanderspek, R., et al. 2015, *Journal of Astronomical Telescopes, Instruments, and Systems*, 1, 014003.  
doi:10.1117/1.JATIS.1.1.014003
- Riener, M., Kainulainen, J., Henshaw, J. D., et al. 2019, *A&A*, 628, A78. doi:10.1051/0004-6361/201935519
- Robertson, J. A. & Eggleton, P. P. 1977, *MNRAS*, 179, 359.  
doi:10.1093/mnras/179.3.359
- Ruciński, S. M. 1969, *AcA*, 19, 245
- Rucinski, S. 2010, *International Conference on Binaries: in celebration of Ron Webbink's 65th Birthday*, 1314, 29.  
doi:10.1063/1.3536391
- Schrijver, C. J. & Zwaan, C. 2000, *Solar and stellar magnetic activity / Carolus J. Schrijver, Cornelius Zwaan*. New York : Cambridge University Press, 2000. (Cambridge astrophysics series ; 34)
- Singh, H. P. & Deb, S. 2011, *16th Cambridge Workshop on Cool Stars, Stellar Systems, and the Sun*, 448, 937
- Shappee, B. J., Prieto, J. L., Grupe, D., et al. 2014, *ApJ*, 788, 48.  
doi:10.1088/0004-637X/788/1/48
- Shaw, J. S. 1994, *Mem. Soc. Astron. Italiana*, 65, 95
- Shokry, A., Saad, S. M., Hamdy, M. A., et al. 2018, *NewA*, 59, 8.  
doi:10.1016/j.newast.2017.08.005
- Sterne, T. E. 1939, *MNRAS*, 99, 451. doi:10.1093/mnras/99.5.451
- Strassmeier, K. G., Hall, D. S., Zeilik, M., et al. 1988, *A&AS*, 72, 291
- Strassmeier, K. G., Hall, D. S., Boyd, L. J., et al. 1989, *ApJS*, 69, 141. doi:10.1086/191310
- Sun, W., Chen, X., Deng, L., et al. 2020, *ApJS*, 247, 50.  
doi:10.3847/1538-4365/ab7894

- Szalai, T., Kiss, L. L., Mészáros, S., et al. 2007, *A&A*, 465, 943.  
doi:10.1051/0004-6361:20066768
- Terrell, D. & Wilson, R. E. 2005, *Ap&SS*, 296, 221.  
doi:10.1007/s10509-005-4449-4
- Traven, G., Feltzing, S., Merle, T., et al. 2020, *A&A*, 638, A145.  
doi:10.1051/0004-6361/202037484
- van Hamme, W. 1993, *AJ*, 106, 2096. doi:10.1086/116788
- von Zeipel, H. 1924, *MNRAS*, 84, 665.  
doi:10.1093/mnras/84.9.665
- Wadhwa, S. S., De Horta, A., Filipović, M. D., et al. 2021, *MNRAS*, 501, 229. doi:10.1093/mnras/staa3637
- Wilson, R. E. & Devinney, E. J. 1971, *ApJ*, 166, 605.  
doi:10.1086/150986
- Wilson, R. E. 1979, *ApJ*, 234, 1054. doi:10.1086/157588
- Wilson, R. E. 1990, *ApJ*, 356, 613. doi:10.1086/168867
- Wu, Y., Luo, A.-L., Li, H.-N., et al. 2011, *Research in Astronomy and Astrophysics*, 11, 924. doi:10.1088/1674-4527/11/8/006
- Wyithe, J. S. B. & Wilson, R. E. 2001, *ApJ*, 559, 260.  
doi:10.1086/322378
- Yang, Y.-G., Zhang, X.-B., Li, H.-L., et al. 2012, *AJ*, 144, 136.  
doi:10.1088/0004-6256/144/5/136
- Yan, H., Li, H., Wang, S., et al. 2022, *The Innovation*, 3, 100224.  
doi:10.1016/j.xinn.2022.100224
- Yang, Y.-G. & Qian, S.-B. 2015, *AJ*, 150, 69.  
doi:10.1088/0004-6256/150/3/69
- Yang, Y. & Wang, S. 2024, *MNRAS*, 531, 3823.  
doi:10.1093/mnras/stae1352
- Zechmeister, M. & Kürster, M. 2009, *A&A*, 496, 577.  
doi:10.1051/0004-6361:200811296
- Zhang, J., Qian, S.-B., Wu, Y., et al. 2019, *ApJS*, 244, 43.  
doi:10.3847/1538-4365/ab442b
- Zhang, B., Li, J., Yang, F., et al. 2021, *ApJS*, 256, 14.  
doi:10.3847/1538-4365/ac0834
- Zhang, L., Zhu, Z., Yue, Q., et al. 2020, *MNRAS*, 491, 6065.  
doi:10.1093/mnras/stz3473
- Zhang, H.-T., Qian, S.-B., Liao, W.-P., et al. 2024, *AJ*, 167, 215.  
doi:10.3847/1538-3881/ad3451
- Zheng, S.-Y., Li, K., & Xia, Q.-Q. 2021, *MNRAS*, 506, 4251.  
doi:10.1093/mnras/stab1829
- Zhou, D. & Leung, K.-C. 1997, *The Third Pacific Rim Conference on Recent Development on Binary Star Research*, 130, 69
- Zhou, X., Qian, S.-B., Essam, A., et al. 2016, *NewA*, 47, 3.  
doi:10.1016/j.newast.2015.12.012
- Zhou, X., Qian, S.-B., Zhang, J., et al. 2016, *ApJ*, 817, 133.  
doi:10.3847/0004-637X/817/2/133
- Zwitter, T., Munari, U., Marrese, P. M., et al. 2003, *A&A*, 404, 333. doi:10.1051/0004-6361:20030446